

# An Updated Corner-Frequency Model for Stochastic Finite-Fault Ground-Motion Simulation

Yuxiang Tang<sup>\*1,2</sup> 

## ABSTRACT

Stochastic finite-fault ground-motion simulation is widely used in various scientific and engineering applications. However, the current theoretical modeling of the corner frequency used in the source spectrum model is problematic as it does not consider the impact of rupture velocity. This article provides a modification of the current corner-frequency modeling and establishes a correlation between corner frequency and rupture velocity, making the source spectrum model more theoretically consistent. An additional inspection of the source-duration model is provided, and the appropriateness of the application of the widely used  $1/f_0$  source-duration model is discussed. A detailed comparison between the updated corner-frequency model and the currently used model (embodied in EXSIM) is provided for various magnitudes. For validation purposes, the updated corner-frequency and source-duration model is applied to predict the ground motions on rock sites during the 2012  $M_L$  5.4 Moe earthquake that occurred in southeastern Australia and the 2014  $M_s$  6.5 Ludian earthquake that occurred in southwestern China. The results show that the updated model is reliable for providing more accurate estimates of corner frequency, source duration, and ground-motion amplitudes with smaller average residuals than the currently used model.

## KEY POINTS

- The currently used corner-frequency models fail to consider the influence of rupture velocity.
- An updated corner-frequency model is proposed and validated by comparing it with EXSIM.
- The newly proposed model is further validated by the ground motions recorded during the 2012 Moe earthquake and the 2014 Ludian earthquake.

## INTRODUCTION

Ground-motion simulation is a reliable approach for generating synthetic accelerograms for various scientific and engineering applications. Recent advances in high-performance computations make the hybrid broadband ground-motion simulation approach, which combines physics-based deterministic simulation at low frequencies ( $<1$  Hz) and stochastic simulation at high frequencies ( $\geq 1$  Hz), more prevalent for seismic hazard assessment (Olsen and Takedatsu, 2015; Jayalakshmi *et al.*, 2021). This approach can obtain more accurate ground-motion estimates due to the improved source characterization and wave-propagation methods. However, pure stochastic ground-motion simulation still plays an important role in estimating ground-

motion levels, especially for low-to-moderate seismicity regions where strong ground motion data are often at a scarcity (e.g., Australia). For example, stochastic ground-motion simulation approach can be used to generate ground motions of engineering interests for a suite of earthquake events rather than a scenario event, and ground-motion model (GMM) (also widely known as GMPE, which is short for ground-motion prediction equation) can be developed from the data set generated by stochastic simulations (Boore, 2009).

The basic principle of the stochastic ground-motion simulation approach is based on the combination of band-limit Gaussian white noise and the deterministic seismological model (Boore, 1983; Atkinson and Boore, 1995). The seismological model is used to define the Fourier amplitude spectrum (FAS) and is usually divided into the source, path, and site components. Two different categories of stochastic ground-motion simulation are identified based on the source model,

1. School of Civil Engineering, Guangzhou University, Guangzhou, China,  <https://orcid.org/0000-0001-6196-598X> (YT); 2. PSE Division, King Abdullah University of Science and Technology, Thuwal, Saudi Arabia

\*Corresponding author: tangyuxiang56@gmail.com

Cite this article as Tang, Y. (2022). An Updated Corner-Frequency Model for Stochastic Finite-Fault Ground-Motion Simulation, *Bull. Seismol. Soc. Am.* **XX**, 1–18, doi: [10.1785/0120210205](https://doi.org/10.1785/0120210205)

© Seismological Society of America

point source (Brune, 1970; Boore, 2003), and finite-fault source (Beresnev and Atkinson, 1998a,b; Motazedian and Atkinson, 2005). The software SMSIM and EXSIM have been developed to implement stochastic point source simulation and finite-fault source simulation, respectively. The two software programs are widely used worldwide for generating synthetic accelerograms for different applications (Atkinson and Boore, 1995, 2006; Allen, 2012; Yenier and Atkinson, 2015; Edwards *et al.*, 2016; Pezeshk *et al.*, 2018). The advantage of EXSIM (finite-fault source), compared with SMSIM (point source), is that it can take the geometric properties and directivity effects of earthquake source into consideration, and thus can simulate ground-motion amplitudes for large earthquakes at near distances more accurately (Motazedian and Atkinson, 2005; Atkinson and Assatourians, 2015).

However, there are several problems with using currently distributed EXSIM (also SMSIM). First, the rupture velocity is not properly considered in the corner-frequency ( $f_0$ ) and source-duration ( $T_0$ , also known as rise time, for small subfaults) model. Because the value of rupture propagation velocity ( $V_{rup}$ ) usually ranges within 0.6 and 1.0 times that of source shear-wave velocity ( $\beta_0$ ) (Beresnev and Atkinson, 1997), the chance that  $V_{rup}$  can influence the directivity of finite-fault radiation and introduce the strong azimuthal dependence on radiation is not high. But  $V_{rup}$  can influence the corner frequency and source duration, obviously (Causse and Song, 2015; Chouhet *et al.*, 2018), especially at short distances, in which the ground-motion duration is largely dominated by the source duration (Boore, 2009). Because there is no proper guidance on the application of  $V_{rup}$  value, this results in a different pre-assumption on driving the corner-frequency model. For example, Brune *et al.* (1979) and Allmann and Shearer (2009) obtained their  $f_0$  model with the assumption that  $V_{rup} = 0.9\beta_0$ , whereas in the currently distributed EXSIM12 and EXSIM\_DMB (this study will use EXSIM in the following context),  $V_{rup} = 0.8\beta_0$ . Second, the derivation of  $T_0$  model varies from study to study. For example, Boore (1983, 2003, 2009) assumed  $T_0 = 1/f_0$ , whereas Boatwright and Choy (1992) assumed  $T_0 = 0.5/f_0$ , and Hough and Dreger (1995) claimed  $T_0 = 0.37/f_0$ . In addition, the original definition of  $T_0$  in EXSIM is  $r/V_{rup}$  (in which  $r$  is the source radius), whereas in Beresnev and Atkinson (1997)  $T_0 = r/2V_{rup}$  (p. 70, equation 13). This difference would significantly influence the source-duration estimation for large events at short distances (in which path duration can be neglected). Therefore, the lack of clear assumptions and ambiguous definitions of the  $f_0$  model and  $T_0$  model would undoubtedly introduce unnecessary uncertainties during the simulation procedures.

This article aims to make fundamental improvements for current practices of implementing stochastic finite-fault ground-motion simulations and make the overall source model more theoretically consistent by modifying the corner-frequency model and the source-duration model. To achieve this goal, the following studies will be conducted in this article:

1. Construct a new corner-frequency model:

The newly constructed  $f_0$  model will incorporate a parameter to reflect the influence of rupture velocity on the corner frequency. A comprehensive comparison between EXSIM (using rupture velocity independent  $f_0$ ) and the newly developed model (using the new rupture velocity dependent  $f_0$ ) will be made for different magnitudes.

2. Perform a re-examination of the source-duration model:

Because the source duration is closely related to the corner frequency (Brune, 1970; Beresnev, 2002), it is required to re-examine it if the  $f_0$  model is modified. This article will examine the source duration of a number of random hypocenters for different magnitudes (different fault sizes) and different source-duration measurements, namely, time duration between the instances of 5% and 95% Arias intensity ( $I_A$ ) ( $T_{5-95}$ ), as well as 5% and 75%  $I_A$  ( $T_{5-75}$ ).

3. Provide example applications of the modified corner-frequency model for validation purpose:

As examples, the newly constructed  $f_0$  model will be applied to predict the ground motions on rock sites during the 2012  $M_L$  5.4 Moe earthquake that occurred in southeastern Australia (SEA) and the 2014  $M_s$  6.5 Ludian earthquake that occurred in southwestern China. The recorded times series of acceleration, peak ground acceleration (PGA),  $I_A$ , 5%-damped pseudoacceleration response spectra (SA), and ground-motion duration (Ludian earthquake only) will be compared with the simulated ones from this study and EXSIM.

The “ $\omega^2$ ” source spectra model is discussed in this study only, and the fault is assumed to be a circular fault during all the derivation procedures.

## REVIEW OF CORNER-FREQUENCY MODELING

As one of the important parameters required in the process of stochastic source modeling of an earthquake event, the corner frequency ( $f_0$ ) controls the amplitude of ground motions at high frequencies (Boore, 1983). Empirically, the corner frequency used in current stochastic simulations is calculated based on the expressions shown by equation (1):

$$f_0 = 4.906 \times 10^6 \beta_0 \left( \frac{\Delta\sigma}{M_0} \right)^{1/3}, \quad (1)$$

in which  $\beta_0$  is the shear-wave velocity at the vicinity of the earthquake source (km/s);  $\Delta\sigma$  is the stress drop (bar); and  $M_0$  is the seismic moment (dyne-cm). During the past five decades, many studies used this expression for various purposes (e.g., Boore, 1983; Atkinson and Boore, 1995; Boore, 2003; Atkinson and Boore, 2006; Boore, 2009; Yenier and Atkinson, 2015). However, none of these studies provide the source or process of how this corner frequency is derived, and the conditions of using this expression are not stated clearly either.

TABLE 1  
Various Assumptions of  $f_0$  Model and  $V_{rup}$  Value in Existing Studies

Number	$V_{rup}$	$f_0$	$T_0$	References
1	/	$0.37(\beta_0/r)$	/	Brune (1970, 1971)
2	$(0.5\text{--}0.9)\beta_0$	$(C_S/2\pi)\beta_0/r$	/	Sato and Hirasawa (1973)
3	$0.9\beta_0$	$0.21(\beta_0/r)$	/	Madariaga (1976)
4	$0.9\beta_0$	$K(\beta_0/r)$ ( $K \approx 1/3$ )	/	Brune <i>et al.</i> (1979)
5	$0.8\beta_0$	/	$0.5/f_0$	Boatwright and Choy (1992)
6	$0.8\beta_0$	/	$0.37/f_0$	Hough and Dreger (1995)
7	$0.8\beta_0$	$(yz/\pi)\beta_0/r$	/	Beresnev and Atkinson (1997, 1998a)
8	$0.8\beta_0$	$0.37(\beta_0/r)$	$1/f_0$	Boore (2003, 2009)
9	$0.9\beta_0$	$0.32(\beta_0/r)$	/	Allmann and Shearer (2009)
10	$0.72\beta_0$	/	$1/f_0$	Irikura and Miyake (2011)
11	$0.9\beta_0$	$0.26(\beta_0/r)$	/	Kaneko and Shearer (2014)

$\beta_0$  refers to source shear-wave velocity;  $C_S$  is a  $y$ -based coefficient;  $r$  is the source radius;  $y$  is the ratio between  $V_{rup}$  and  $\beta_0$ ;  $z$  is the parameter defining the strength of high-frequency radiation.

According to Kanamori and Anderson (1975), the seismic moment of a circular fault can be expressed by the magnitude of the event (detailed information is given in Kanamori and Anderson, 1975, p. 1082); therefore, the fault dimension can be expressed by equation (2):

$$M_0 = \frac{16}{7} \Delta\sigma r^3, \quad (2)$$

in which  $r$  is the source radius.

Then, the source radius can be expressed by equation (3):

$$r = \left( \frac{7M_0}{16\Delta\sigma} \right)^{1/3}. \quad (3)$$

In addition, Brune (1970, 1971) shows that

$$2\pi f_0 = 2.34\beta_0/r. \quad (4)$$

Then, the source radius can also be expressed by equation (5):

$$r = \frac{2.34\beta_0}{2\pi f_0}. \quad (5)$$

By combining equations (3) and (5), one can get equation (6):

$$f_0 = 0.4906\beta_0 \left( \frac{\Delta\sigma}{M_0} \right)^{1/3}. \quad (6)$$

If we change all the parameters from SI units to the same units as equation (1), factor  $10^7$  should be added into equation (6), which will lead to equation (1) accordingly.

By contrast, according to Allmann and Shearer (2009), equation (7) is used instead of equation (4):

$$f_0 = 0.32\beta_0/r, \quad (7)$$

which leads to equation (8) when combining it with equation (3):

$$f_0 = 0.4215\beta_0 \left( \frac{\Delta\sigma}{M_0} \right)^{1/3}. \quad (8)$$

The detailed deriving process of equation (7) is not given, and the rupture velocity is assumed to be  $0.9\beta_0$  in the study (Allmann and Shearer, 2009).

Even though both equations (6) and (8) provide the correlation between corner frequency and stress drop (as equation 8 is not widely used, this study focuses on equation 6 only), the pre-assumption of the rupture velocity value is neglected by many researchers. Some may argue that the value of stress-drop value can reveal the rupture velocity value as there is a fundamental trade-off between them, and the variations of stress drop can be interpreted as the variations of rupture velocity. However, in the practical application, the rupture velocity value is often assumed to be inherently constant (i.e.,  $0.8\beta_0$ ), which is not corresponding to equation (6) (Beresnev and Atkinson, 1997; Lam *et al.*, 2000). Therefore, it is required to take the rupture velocity into consideration in corner-frequency modeling to make the source model more theoretically consistent.

To illustrate the large variances of the corner-frequency modeling more clearly, a summary of existing studies related to  $f_0$  model and  $V_{rup}$  assumption is shown in Table 1.

As shown in Table 1, there is a pre-assumption of rupture velocity value for each corner-frequency model. However, the currently used corner-frequency model in EXSIM neglects the assumption and sets the rupture velocity somewhat arbitrarily without changing the value of the corner frequency itself. This conflict would inevitably introduce extra uncertainties in estimating the ground-motion levels.

## UPDATED CORNER-FREQUENCY MODEL

In this section, the author aims to derive the corner-frequency model step-by-step based on previous studies and provide the very fundamental updated expression of corner frequency, which takes rupture velocity into consideration for more rigorous applications.

According to Beresnev and Atkinson (1997), the far-field shear-wave displacement can be expressed by equation (9):

$$\mathbf{u}(\mathbf{x}, t) = \frac{\mathbf{R}^{\theta y}}{4\pi\rho_0\beta_0^3 R} \mu A \bar{u}'(t - R/\beta_0), \quad (9)$$

in which  $\mathbf{u}(\mathbf{x}, t)$  is the displacement at the point  $\mathbf{x}$  at time  $t$ ;  $\rho_0$  and  $\beta_0$  are the density and shear-wave velocity at the vicinity of seismic source, respectively;  $\mathbf{R}^{\theta y}$  indicates the angular radiation pattern;  $\mu$  is the shear modulus;  $A$  is the whole area of the dislocation;  $\bar{u}'$  is the time derivation of the average displacement across the dislocation plane; and  $R$  is the distance. For convenience, the unit of each parameter will not be given during the modeling process.

According to the boundary condition, the displacement must start from 0 and approach to  $\bar{u}'(\infty)$  over the source duration (also called rise time for small subfault sources)  $T_0$ . Two reasonable ad hoc time functions satisfying the boundary condition provided by Beresnev and Atkinson (1997) are shown in equations (10) and (11):

$$\bar{u}_1(t) = \bar{u}(\infty)[1 - (1 + t/\tau)e^{-t/\tau}], \quad (10)$$

$$\bar{u}_2(t) = \frac{\bar{u}(\infty)}{2}\{2 - [1 + (1 + t/\tau)^2]e^{-t/\tau}\}, \quad (11)$$

in which  $\tau$  is the characteristic time parameter for controlling the increasing rate of displacement;  $\bar{u}_1(t)$  and  $\bar{u}_2(t)$  are two of the infinite number of ad hoc time functions satisfying the boundary condition; and  $\bar{u}(\infty)$  represents a certain level of displacement over the source duration. The derivatives of equations (10) and (11) can be expressed by equation (12):

$$\bar{u}'_n = \frac{\bar{u}(\infty)}{n!\tau} \left(\frac{t}{\tau}\right)^n e^{-t/\tau}. \quad (12)$$

Equation (13) can be obtained by substituting equation (12) into (9):

$$\mathbf{u}_n(\mathbf{x}, t) = \frac{\mathbf{R}^{\theta y} M_0}{4\pi\rho_0\beta_0^3 \tau R n!} \left(\frac{t - R/\beta_0}{\tau}\right)^n e^{-(t-R/\beta_0)/\tau}, \quad (13)$$

in which  $M_0 = \mu A \bar{u}(\infty)$ .

The modulus of the vector obtained from the Fourier transform of equation (13) is shown in equation (14):

$$|\mathbf{u}_n(\mathbf{x}, \omega)| = \frac{\mathbf{R}^{\theta y} M_0}{4\pi\rho_0\beta_0^3 R} (1 + \omega/\omega_0)^{-(n+1)/2}, \quad (14)$$

in which  $\omega_0 = 1/\tau$ .

As mentioned earlier, the source spectrum discussed in this study is only for the “ $\omega^2$ ” form, therefore  $n = 1$  in equations (12), (13), and (14), and equation (10) can be used to represent the boundary condition. The source duration can be defined as the time during which the average slip reaches a certain fraction  $x$  of  $\bar{u}(\infty)$  as the slip duration in equation (10) is unlimited. Therefore, equation (15) is obtained from equation (10) with the introduction of  $x$ , and it can be used to link the source duration and slip fraction:

$$(1 + z)e^{-z} = 1 - x, \quad (15)$$

in which  $z$  is the parameter defining the strength of high-frequency radiation and  $z = T_0/\tau$ . According to equation (15), the  $x$  value would impact the source-duration modeling fundamentally. For example, if  $x = 0.5$  (which means the average slip reaches 50% of the final slip  $\bar{u}(\infty)$ ), then  $z = 1.68$ , and  $T_0$  would be  $0.27/f_0$ ; by contrast, if  $T_0 = 1/f_0$  (Boore, 1983, 2009), then  $z = 6.28$ , and  $x = 0.986$  (which means the average slip reaches almost 100% of  $\bar{u}(\infty)$ ).

The source duration can also be related to the fault dimension, namely, the fault radius  $r$ . If the rupture velocity is assumed to be  $V_{\text{rup}} = y\beta_0$  ( $0 < y < 1$ ), then the source duration can be calculated using equation (16) approximately (Beresnev and Atkinson, 1997; Lam et al., 2000):

$$T_0 = \frac{r}{2V_{\text{rup}}} = r/(2y\beta_0). \quad (16)$$

The equation (16) is obtained based on the assumption that slip at every point on the subfault continues until the rupture reaches its periphery and stops (Beresnev and Atkinson, 1997), and the average rupture propagates half of the distance  $r$  (i.e., a rupture from the middle of the fault), and this is not related to  $x$ .

In addition,

$$T_0 = z/\omega_0 = z/(2\pi f_0). \quad (17)$$

Based on equations (16) and (17), the corner frequency can be expressed by equation (18):

$$f_0 = \left(\frac{yz}{\pi}\right)\beta_0/r. \quad (18)$$

Equation (18) is also shown in Beresnev and Atkinson (1997) (equation 14, p. 70) and Beresnev and Atkinson (1998a, equation 1, p. 1393).

Substituting equation (3) into (18), the final corner frequency can be expressed by equation (19a):

$$f_0 = 0.42yz\beta_0 \left(\frac{\Delta\sigma}{M_0}\right)^{1/3}, \quad (19a)$$

in which all the parameters are expressed in consistent SI units; if  $\beta_0$  is expressed in km/s,  $\Delta\sigma$  is in bars, and  $M_0$  is in dyne-cm, then equation (19a) needs to be changed into equation (19b):

$$f_0 = 4.2 \times 10^6 yz\beta_0 \left( \frac{\Delta\sigma}{M_0} \right)^{1/3}. \quad (19b)$$

The expressions developed by Brune (1970, 1971) suggest that  $y = 0.69$  (which means the rupture velocity is 0.69 times the shear-wave velocity  $\beta_0$ ) (Lam *et al.*, 2000), and the common convention is to define the rise time as corresponding to the average slip reaching 50% of the slip across the dislocation plane ( $x = 0.5$ ). Using equations (18) and (19b), the final corner frequency can be expressed by equation (20):

$$f_0 = (0.69 \times 1.68/\pi)\beta_0/r = 0.37\beta_0/r, \quad (20a)$$

and

$$\begin{aligned} f_0 &= 4.2 \times 10^6 \times 0.69 \times 1.68\beta_0 \left( \frac{\Delta\sigma}{M_0} \right)^{1/3} \\ &= 4.869 \times 10^6 \beta_0 \left( \frac{\Delta\sigma}{M_0} \right)^{1/3}. \end{aligned} \quad (20b)$$

Equation (20a) corresponds to equation (4) exactly, and equation (20b) corresponds to equation (1) closely. This means the pre-assumption of  $y = 0.69$  and  $x = 0.5$  is valid, and we can obtain Brune's corner-frequency model (Brune, 1970, 1971) accordingly.

By contrast,  $y$  is often set as 0.8 in the currently distributed EXSIM (Beresnev and Atkinson, 1998a,b; Atkinson and Boore, 2006; Boore, 2009; etc.), and according to equation (19), the corresponding corner frequency is (with  $x = 0.5$ ):

$$f_0 = 5.645 \times 10^6 \beta_0 \left( \frac{\Delta\sigma}{M_0} \right)^{1/3}. \quad (21)$$

Equation (21) is quite different from equation (1), which is widely adopted in current studies. Therefore, the conditions of using equation (1) in stochastic simulation procedures should be strictly stated.

Figure 1 shows the influences of slip fraction ( $x$ ) and rupture velocity ( $y$ ) on the value of  $f_0$ .

Apparent impacts of both slip fraction and rupture velocity on the value of corner frequency can be found in Figure 1. As

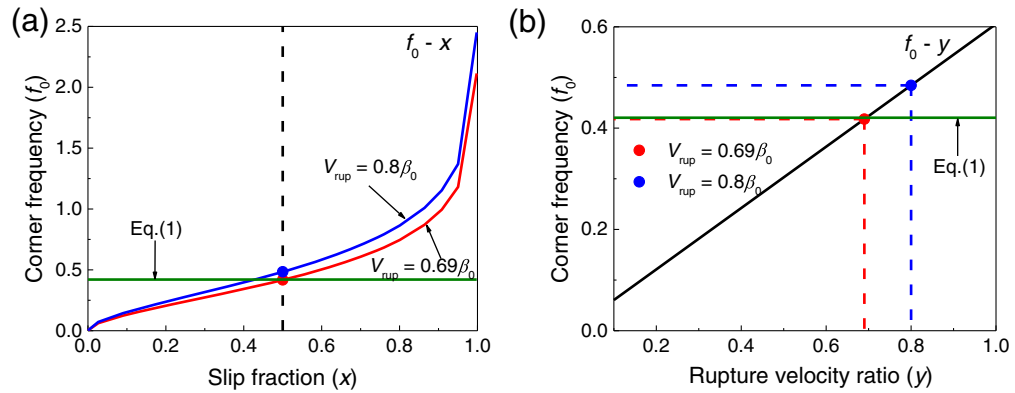


**Figure 1.** Influences of (a) slip fraction ( $x$ , with  $y = 0.69$  and 0.8) and (b) rupture velocity ratio ( $y$ , with  $x = 0.5$ ) on corner frequency ( $f_0$ ), using equation (19).  $\Delta\sigma = 140$  bars and  $\mathbf{M} = 6$ . The color version of this figure is available only in the electronic edition.

normally, the slip fraction is set to be 0.5 (Beresnev and Atkinson, 1997), and this study will focus on the effect of rupture velocity only in the next sections. Multiple simulations are performed to show the effect of rupture velocity on the FAS for different magnitudes. The input parameters for the simulations are listed in Table 2.

The results are shown in Figure 2. As shown in Figure 2,  $y = 0.69$  can obtain a very close estimation of corner frequency and FAS with EXSIM, whereas  $y = 0.8$  would obtain higher corner frequency and FAS at frequencies above corner frequency for all magnitudes, indicating that the choice of rupture velocity would impact the corner frequency and Fourier amplitude significantly.

## RE-EXAMINATION OF SOURCE-DURATION MODEL

The original source duration in the currently distributed versions of EXSIM is calculated by equation (22):

$$T_0 = \frac{r}{V_{rup}} = \frac{\sqrt{dl \times dw/\pi}}{V_{rup}}, \quad (22)$$

in which  $dl$  and  $dw$  are the length and width of the subfault used in the simulations.

Boore (2009) suggested the source duration can be modeled using  $1/f_0$ , and this model is widely adopted by the researchers world around. However, to make the overall source model more theoretically consistent, this study suggests using equation (16) rather than equation (22) to calculate  $T_0$ . Therefore, it is necessary to re-examine whether the source-duration model ( $1/f_0$ ) is suitable for use any longer. In this study, the author takes the suggestion given by Boore (2009) and only considers the pulsing subfault case as it is more physical than the static subfault case. Because it is controversial whether to use the 90% ground-motion duration (time between the instances of 5% and 95%  $I_A$ ) (Allen, 2012; Dang and Liu, 2020) or 70%

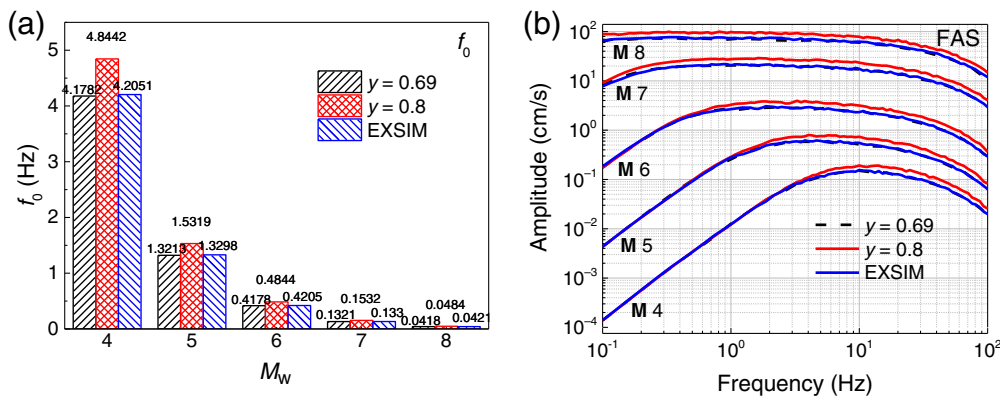


**Figure 2.** Influences of (a) rupture velocity on corner frequency ( $f_0$ ) and (b) Fourier amplitude spectrum. In currently distributed EXSIM, the corner frequency is computed using equation (1) and  $V_{\text{rup}} = 0.8\beta_0$ ; the corner frequency in other situations is computed using equation (19). The rupture distance between the example site and the reference source point for **M** 4–8 is 44.26, 42.27, 35.19, 11.04, and 6.87 km. The detailed information about the software program (named Ground-Motion Simulation System Version 2.0 [GMSS2.0]) used for generating the spectra can be found in [Data and Resources](#). The color version of this figure is available only in the electronic edition.

TABLE 2  
Input Parameters for Simulations

Parameter	Value
Time step, $dt$ (s)	0.002
Source density, $\rho_0$ (g/cm <sup>3</sup> )	2.8
Source shear-wave velocity, $\beta_0$ (km/s)	3.7
Fault orientation, strike, dip, rake (°)	3, 29, 45
Fault dimension along strike and dip (km)	Wells and Coppersmith (1994)
Subfault dimension (km)	$2 \times 2$
Location of reference point, latitude, longitude (°)	23.617, 120.689
Reference depth (km)	0.94
Moment magnitude, $M_w$ (dyne-cm)	4.0–8.0
Stress drop, $\Delta\sigma$ (bar)	140
Reference stress drop, $\Delta\sigma$ (bar)	70
Window function	Saragoni and Hart (1974), with the value of the parameters given in Boore (2009)
Rupture velocity, $V_{\text{rup}}$ (km/s)	$0.69\beta_0, 0.8\beta_0$
Slip fraction, $x$	0.5
Slip distribution	Random
Pulsing percentage (%)	50
Source duration, $T_0$	$r/V_{\text{rup}}$ (EXSIM), $r/2V_{\text{rup}}$ (this study)
Path duration	$0.05 \times R$
Geometric spreading	$R^{-1.3}$ ( $0 < R \leq 70$ ) $R^{0.2}$ ( $70 < R \leq 140$ ) $R^{-0.5}$ ( $140 < R$ ) $\max(1000, 893f^{0.32})$
Quality factor	
Crust and site amplification	1.0
$\kappa_0$ (s)	0.005
Location of the sample site, latitude, longitude (°)	24, 120.8333
Number of simulations per hypocenter	20
Number of random hypocenters	20

$$G(R_{\text{eff}})e^{-\pi f_q R_{\text{eff}}/(Q(f_q)C_q)}$$

$$= \sqrt{\sum_i^{\text{nl}} \sum_j^{\text{nw}} [G(R_{ij})e^{-\pi f_q R_{ij}/(Q(f_q)C_q)}]^2} / (\text{nl} \times \text{nw}), \quad (23)$$

in which,  $G(R)$  and  $Q(f)$  are the geometric spreading function and quality factor given in Table 2;  $f_q$  is the reference frequency, and 10 Hz is adopted in this study (Boore, 2009);  $C_q$  is the crustal shear-wave velocity factor, and 3.7 km/s is adopted in this study; nl and nw are the number of subfault along strike and down dip. Other parameters are listed in Table 2.

For different scenarios (magnitudes), the size of the fault (nl and nw) is different. The effective distance calculated by equation (23) for this study is 39.1, 22.0, and 20.6 km for **M** 6, 7, and 8, respectively. These values are validated by Boore's program, which is named " $r_{\text{eff}}$ ," with the values 39.72, 21.29, and 20.43 km, respectively (see [Data and Resources](#)). These distances are not short enough to neglect the influence on the whole duration (the path duration for each distance is 1.96, 1.1, and 1.03 s, respectively). Therefore, it is necessary to remove the path duration from the whole duration calculated from the Husid plot. Figure 3 shows the time series alongside the normalized Husid plot for three magnitudes (one random simulation), and Figure 4 shows the durations for each magnitude, alongside the two options for calculating source duration ( $0.27/f_0$  and  $1/f_0$ ).

For the **M** 6 situation in Figure 4, as the distance is long enough to dominate the whole duration, there are some fundamental uncertainties in estimating the real source duration (source duration) by subtracting the path duration from the overall duration, and thus some source-duration estimations in Figure 4 are less than 0 (for 75%–5% level only). Figure 4 also shows that the smaller  $R_{\text{eff}}$  can make the source-duration

duration (time between the instances of 5% and 75%  $I_A$ ) (Ou and Herrmann, 1990; Boore, 2009) as the ground-motion duration, this study will examine the source-duration model for both conditions.

To consider the source duration more accurately, the path duration was removed from the whole duration in the first place. The effective distance ( $R_{\text{eff}}$ ) rather than rupture distance ( $R_{\text{rup}}$ ) is used to calculate the path duration, which is suggested by Boore (2009). Equation (23) is used for finding the  $R_{\text{eff}}$  value for each scenario:

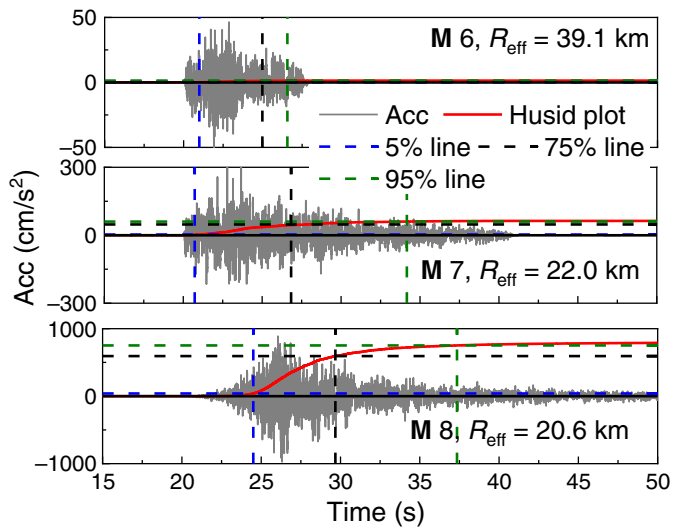


**Figure 3.** Example acceleration time series for **M 6, 7, and 8** earthquakes. The dashed lines indicate the percentage of the Husid plot (5%, 75%, and 95%) and the corresponding time. The color version of this figure is available only in the electronic edition.

estimations less scattered, and this result is supported by Boore (2009) (in which  $R_{\text{eff}} = 10.3$  and  $6.7$  km are adopted, and less scatter source duration was obtained).

Figure 4 illustrates that the  $1/f_0$  model significantly overestimates  $T_0$  if  $T_{5-75}$  is taken as the whole duration  $T_d$ , which is not supported by Boore (2009). In addition, the  $1/f_0$  model can give a higher estimation of  $T_0$  if  $T_{5-95}$  is taken as the  $T_d$ , especially for a large event (short effective distance). Interestingly, according to the simulations conducted by this study, the  $0.6/f_0$  model can give roughly close estimations of source duration if  $T_{5-95}$  is taken as the  $T_d$ . This result is in agreement with the assumption that 90% of static displacement is reached ( $x = 0.9$ ) using equation (15) (more detailed derivation can be found in Beresnev, 2002, p. 2048).  $0.27/f_0$  gives apparent underestimates of  $T_0$  for the 95%–5% level but can get close estimates of  $T_0$  for the 75%–5% level (especially for short effective distance). Considering there is a growing trend to use  $T_{5-75}$  rather than  $T_{5-95}$  for calculating  $T_d$  (Bahrampouri et al., 2021), this study suggests using  $0.27/f_0$  as the basic formulae for calculating source duration.

## EXAMPLE APPLICATIONS

This section will illustrate the application of the newly proposed corner-frequency and source-duration model in simulating the ground motions on rock sites during the Moe earthquake (19 June 2012  $M_L$  5.4) and the Ludian earthquake (3 August 2014  $M_s$  6.5). The 2012 Moe earthquake occurred in Victoria, SEA, located nearly 130 km southeast of Melbourne. Detailed studies of the Moe earthquake have been conducted during the past decade (Australian Energy Market Operator [AEMO], 2013; Sandiford, 2013; Hoult et al., 2014;

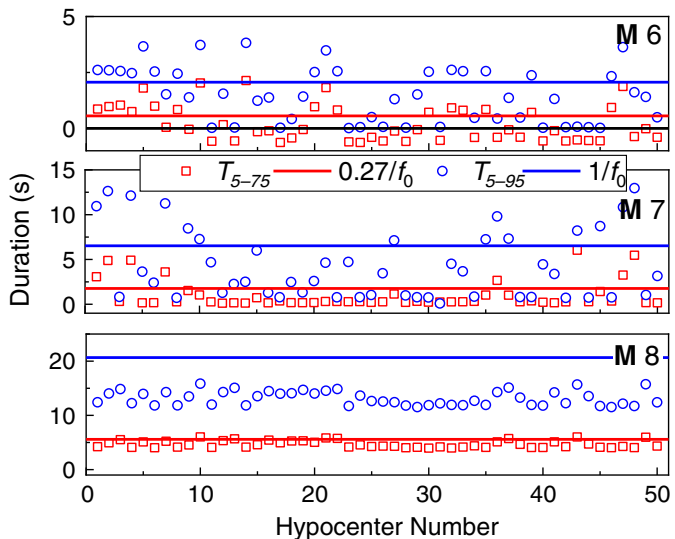


**Figure 4.** Durations between 75%–5% ( $T_{5-75}$ ) and 95%–5% ( $T_{5-95}$ ) levels and on normalized Husid plots, and two options to calculate source duration using corner frequency ( $0.27/f_0$  and  $1/f_0$ ). Equation (16) is used for calculating source duration in the program. The durations are averages of 20 random simulations over 50 random hypocenters. The path durations ( $T_p$ ) have been removed from the original durations ( $T_d$ ). The color version of this figure is available only in the electronic edition.

Attanayake et al., 2019; Hoult et al., 2021). The 2014 Ludian earthquake occurred at the junction of Sichuan, Yunnan, and Guizhou provinces in southwest China. Several agencies and independent scholars from China and other countries have studied this earthquake thoroughly (Liu et al., 2014; Zhao et al., 2014; Cheng et al., 2015; Xie et al., 2015; Xu et al., 2015; Zhang et al., 2015; Cheng et al., 2016; Li and Wang, 2019). This section aims to validate the updated corner-frequency model by comparing the simulated ground motions from GMSS2.0 (which is short for Ground-Motion Simulation System Version 2.0, a software program that embodied the proposed corner-frequency and source-duration model by this study, Tang, 2021, and Tang et al., 2021) and currently distributed EXSIM with the recorded ones from field measurements.

For the 2012 Moe earthquake, there are 87 accelerograms recorded by 33 stations (6 of which only recorded vertical component motions), and 22 stations are on rock site condition (with  $V_{S30} > 620$  m/s) and the rest 11 stations are on soil site (with  $V_{S30} \leq 620$  m/s) (Hoult et al., 2021). For the 2014 Ludian earthquake, there are 237 accelerograms recorded by 79 stations in total till now, among which 8 stations are on rock site condition. Because the complicated site effects of soil sites cannot be accurately estimated without the detailed local geological surveys such as seismic-wave profiles, the accelerograms recorded from soil sites are not considered in this study. For simplicity, only the ground motions on rock sites and within the epicentral distance range 0–300 km are considered

TABLE 3

**Detailed Information of the Considered Stations for the 2012 Moe Earthquake**

Number	Station	Latitude (°)	Longitude (°)	$R_{\text{epi}}$ (km)	Azimuth (°)	$R_{\text{eff}}$ (km)	PGA (cm/s²)	
							HNE	HNN
1	KRAN	-38.359	145.848	37.79	256.385	41.11	10.290	9.016
2	TOMM	-37.809	146.350	52.74	7.729	57.23	91.728	76.146
3	FSHM	-38.757	146.000	58.08	203.764	59.74	5.096	5.782
4	TOO	-37.571	145.491	104.18	319.082	107.50	1.550	1.831
5	DROM	-38.348	144.960	114.46	266.157	118.81	7.546	6.762
6	MLWM	-37.136	145.512	143.48	332.348	144.98	7.154	6.272
7	ROWM	-37.806	144.292	180.94	286.899	181.10	5.39	3.332
8	S88U	-37.168	144.052	230.82	302.358	231.12	1.372	1.274

PGA, peak ground acceleration.

 $R_{\text{epi}}$  and Azimuth are calculated using the software program Ground-Motion Simulation System Version 2.0, and  $R_{\text{eff}}$  is calculated using equation (23).

TABLE 4

**Detailed Information of the Considered Stations for the 2014 Ludian Earthquake**

Number	Station	Latitude (°)	Longitude (°)	$R_{\text{epi}}$ (km)	Azimuth (°)	$R_{\text{eff}}$ (km)	PGA (cm/s²)	
							EW	NS
1	53LDC	27.200	103.599	26.59	67.89	40.10	45.870	44.878
2	53ZTT	27.299	103.699	40.41	58.66	53.20	9.412	8.565
3	53QJT	26.899	102.900	50.38	242.24	55.50	24.770	20.594
4	53DTB	26.399	103.000	86.36	203.73	74.00	16.470	16.541
5	53DTD	26.200	103.099	104.22	193.85	88.50	6.542	5.319
6	53SFX	28.600	104.400	195.20	31.92	209.74	2.916	2.296
7	51YBY	29.000	104.599	243.28	30.25	257.91	1.891	2.425
8	51LZT	28.899	105.400	282.97	45.33	293.86	2.014	1.646

PGA, peak ground acceleration.

 $R_{\text{epi}}$  and Azimuth are calculated using the software program Ground-Motion Simulation System Version 2.0, and  $R_{\text{eff}}$  is calculated using equation (23).

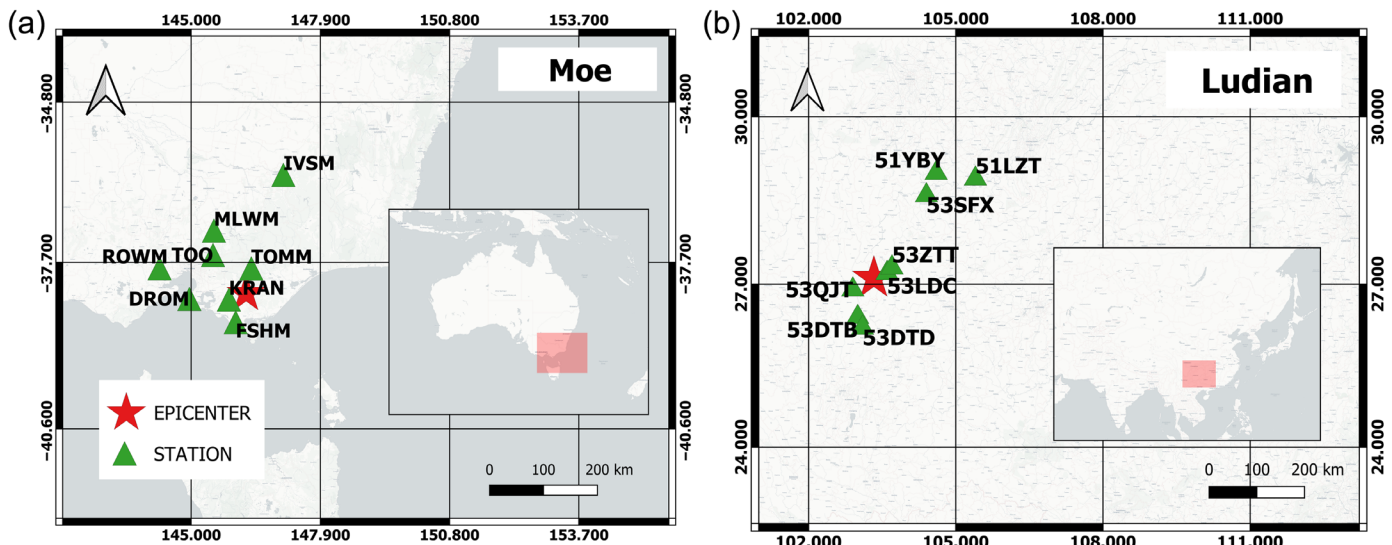
for both events in this study. The detailed information of the selected stations on the rock site is given in Tables 3 and 4 for the 2012 Moe earthquake and the 2014 Ludian earthquake, respectively, and the station maps are shown in Figure 5.

To determine the site response for each station, the widely used horizontal-to-vertical component spectral ratio (HVSR) approach is adopted in this study for both events (Zhu *et al.*, 2020). Various studies have shown that the HVSR approach is reliable for estimating the local site response for rock sites (e.g., Atkinson and Boore, 2006; Allen, 2012). The calculated frequency-dependent amplification factors for the 2012 Moe earthquake and the 2014 Ludian earthquake are shown in Figure 6a and 6b, respectively.

Comprehensive reviews of previous studies are conducted to determine suitable values of input parameters of the simulations for both events. As for the 2012 Moe earthquake, the geometric spreading function is adopted from Allen *et al.* (2007) as it is specific for SEA, and both Attanayake *et al.* (2019) and Hoult *et al.* (2021) use Allen *et al.* (2007) model to determine the source parameters for this event. To avoid any additional trade-offs between the geometric spreading

function and anelastic attenuation function (Edwards *et al.*, 2016), the anelastic attenuation function is also adopted from Allen *et al.* (2007). The three-segment  $T_{5-95}$  path duration model is adopted from Allen (2012) as this model is more comprehensively modeled using a large data set for SEA. The stress drop and magnitude are adopted from Hoult *et al.* (2021) (290 bars and  $M_w$  5.1 on average) as it removed the recording data caught by temporary stations and stations away from mainland Australia, and therefore the estimated value of stress drop and magnitude can be more appropriate than those given by Attanayake *et al.* (2019) (570 bars and  $M_w$  4.9 on average).

For the 2014 Ludian earthquake, the geometric spreading function and anelastic attenuation model are both adopted from Xu *et al.* (2010) as this model is proposed specifically for Yunnan and Sichuan regions, and this model is supported by other studies (e.g., Su, 2009). The five-segment  $T_{5-95}$  path duration model is adopted from Wang *et al.* (2021) because this model is modeled from a data set containing a large number of events that occurred in Sichuan province. The stress-drop value is adopted from Liu *et al.* (2014), which is obtained from the inversion analysis of regional broadband data of this



event. Compared with other studies, including Wang (2017) (which uses 40 bars) and Li and Wang (2019) (which uses 50 bars), Liu *et al.* (2014) is more suitable in this study as this value (28 bars) is supported by the latest study (Wang *et al.*, 2021) (which uses 30 bars). For both events, the average kappa value ( $\kappa_0$ ) is obtained from the average value of the selected stations on rock sites.

The overall input parameters for simulations are summarized in Table 5.

The results are shown in Figures 7–13, in which Figure 7 shows the recorded and simulated time series for the 2012 Moe event; Figure 8 shows the same content for the 2014 Ludian event; Figure 9 shows the recorded and simulated PGA and  $I_A$  for both events; Figures 10 and 11 show the recorded and simulated 5%-damped SA for the 2012 Moe event and the 2014 Ludian event, respectively; Figure 12 shows the residuals of SA between recordings and simulations; and Figure 13 shows the recorded and simulated durations (for the 2014 Ludian earthquake only).

The simulated acceleration time series shown in Figures 7 and 8 can generally represent the amplitude of the recorded time series for all sites. Therefore, the results demonstrate that the parameters listed in Table 5 are suitable for simulating the ground motions on rock sites for both events. The residual between the recorded ground motions and the simulated ones is defined by equation (24) in this study:

$$Re = \ln(GM_R/GM_S), \quad (24)$$

**Figure 5.** Distribution of selected strong-motion stations of (a) the 2012 Moe earthquake and (b) the 2014 Ludian earthquake. Only ground motions recorded by stations on rock site and within the distance range of 0–300 km are considered in this study. The color version of this figure is available only in the electronic edition.

in which  $Re$  is the residual,  $GM_R$  stands for the medium recorded ground motions, and  $GM_S$  is the simulated ones. The ground motions include PGA,  $I_A$ , and 5%-damped SA in this study.

For both events,  $I_A$  is compared as this intensity measures the strength of ground motion, and it is a reliable parameter to describe the ground shaking level (Bahrampouri *et al.*, 2021). In Figure 8a, the results show that the simulated PGA and  $I_A$  by GMSS2.0 (this study) are very close to the recordings, and the average residual is less than 0.2 and 0.4 for PGA and  $I_A$ , respectively, indicating that GMSS2.0 can give the ground-motion estimates with a reasonable level of accuracy.

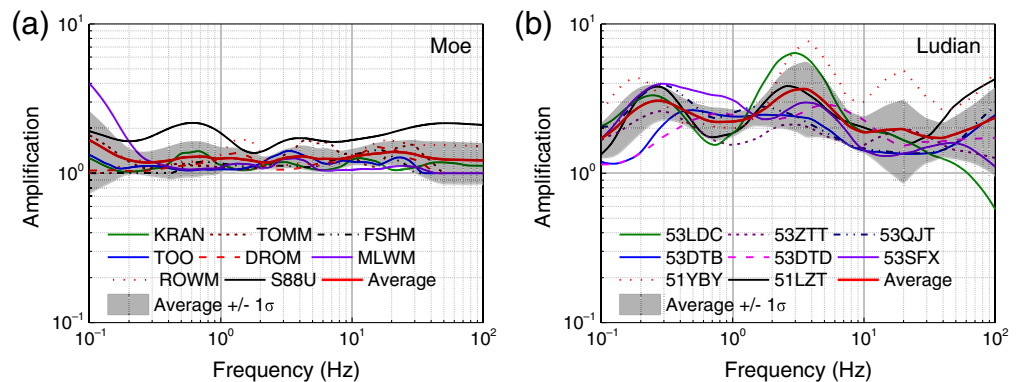


**Figure 6.** Site amplification factors on rock sites for the (a) Moe and (b) Ludian earthquakes, which are calculated using the horizontal-to-vertical component spectral ratio approach. The color version of this figure is available only in the electronic edition.

TABLE 5  
Parameters Used for Simulating the Moe and Ludian Earthquakes

Input Parameter	2012 Moe Earthquake	2014 Ludian Earthquake
Time step, $dt$ (s)	0.004 (this study)	0.005 (this study)
Source density, $\rho_0$ ( $\text{g}/\text{cm}^3$ )	2.8 (Allen, 2012)	2.8 (Liu et al., 2014)
Source shear-wave velocity, $\beta_0$ ( $\text{km}/\text{s}$ )	3.6 (Allen, 2012)	3.5 (Liu et al., 2014)
Fault orientation, strike and dip ( $^\circ$ )	218, 78 (Attanayake et al., 2019)	165, 86 (Zhang et al., 2015)
Fault dimension along strike and dip (km)	2.95, 2.75* (Leonard, 2010)	42, 20 (Wang, 2017)
Subfault dimension (km)	1.5 $\times$ 1.5 (this study)	2 $\times$ 2 (this study)
Location of reference point, latitude, longitude ( $^\circ$ )	-38.279, 146.269 (Hoult et al., 2021)	27.11, 103.35 (Wang et al., 2021)
Reference depth (km)	17.2 (Hoult et al., 2021)	10.0 (Wang, 2017)
Moment magnitude, $M_w$ (dyne-cm)	5.1 (Hoult et al., 2021)	6.1 (Xie et al., 2015)
Stress drop, $\Delta\sigma$ (bar)	290 (Hoult et al., 2021)	28 (Liu et al., 2014)
Window function	Saragni and Hart (1974)	Saragni and Hart (1974)
Rupture velocity, $V_{\text{rup}}$ ( $\text{km}/\text{s}$ )	0.9 $\beta_0$ (Attanayake et al., 2019)	0.8 $\beta_0$ (Wang et al., 2021)
Path duration	0.00 ( $0 < R \leq 10$ ) 0.14 $\times R$ ( $10 < R \leq 70$ ) -0.04 $\times R$ ( $70 < R \leq 160$ ) 0.07 $\times R$ ( $R > 160$ km) (Allen, 2012)	0.2 $\times R$ ( $0 < R \leq 50$ ) 0.075 $\times R$ ( $50 < R \leq 90$ ) -0.0031 $\times R$ ( $90 < R \leq 250$ ) 0.064 $\times R$ ( $250 < R \leq 320$ ) 0.145 $\times R$ ( $R > 320$ ) (Wang et al., 2021)
Geometric spreading	$R^{-1.3}$ ( $0 < R \leq 90$ ) $R^{0.1}$ ( $90 < R \leq 160$ ) $R^{-1.6}$ ( $R > 160$ ) (Allen et al., 2007)	$R^{-1.0}$ ( $0 < R \leq 50$ ) $R^{-0.3}$ ( $50 < R \leq 90$ ) $R^{-1.1}$ ( $90 < R \leq 120$ ) $R^{-0.5}$ ( $R > 120$ ) (Xu et al., 2010)
Quality factor	max (1000, $363f^{0.48}$ ) (Allen et al., 2007)	$180f^{0.5}$ (Xu et al., 2010)
Average $\kappa_0$ (s)	0.02 (this study)	0.022 (this study)
Slip fraction, $x$	0.5 (Beresnev and Atkinson, 1997)	
Pulsing percentage (%)	50 (Boore, 2009)	
Number of simulations per hypocenter	20 (this study)	
Number of random hypocenters	50 (this study)	

\*The dimension is calculated using Leonard's empirical relationship for the stable continental region.

Similarly, the PGA and  $I_A$  shown in Figure 8b indicate that the simulated PGA and  $I_A$  by GMSS2.0 are very close to the recorded ones for all sites, and the average residuals of GMSS2.0 simulations for PGA and  $I_A$  are both less than 0.05, indicating that the accuracy level is acceptable. By contrast, the predictions of EXSIM are generally underestimated as the corner frequency used by EXSIM is smaller than that used by GMSS2.0, resulting in the overall simulated intensities being smaller and the residuals larger.

The simulated SA by GMSS2.0 can match the recorded SA with a reasonable accuracy level for all sites, demonstrated by the average residuals shown in Figure 11. For both the Moe earthquake and Ludian earthquake, GMSS2.0 performs better than EXSIM in simulating the SA, as evidenced by the fact that the average residual of GMSS2.0 is smaller than that of EXSIM at all periods.

To investigate the accuracy of different duration models, the overall duration  $T_{5-95}$  (time between the instances of 5% and

95%  $I_A$ ) is calculated for both recorded and simulated ground motions at each site. Because the original information about the source fault is not available for the 2012 Moe earthquake, and the estimated fault dimensions contain large uncertainties, the simulated duration can be biased to a large extent. For example, the simulated  $T_{5-95}$  for the 2012 Moe earthquake (6.9 s on average) can be three times smaller than the duration calculated from the recording accelerograms (22.3 s on average). Therefore, only the 2014 Ludian earthquake is shown in Figure 13. Because the path duration given in Table 5 is derived based on the assumption that  $T_{5-95} = T_d$ , only  $T_{5-95}$  is discussed in this section.

Because the path duration model is derived for the average condition for Yunnan and Sichuan regions, the author assumes this model is reliable to model the path duration for the 2014 Ludian earthquake. Figure 13a reveals that for distances less than 100 km (including 53LDC, 53ZTT, 53QJT, 53DTB, and 53DTD stations), the duration given by EXSIM is intuitively

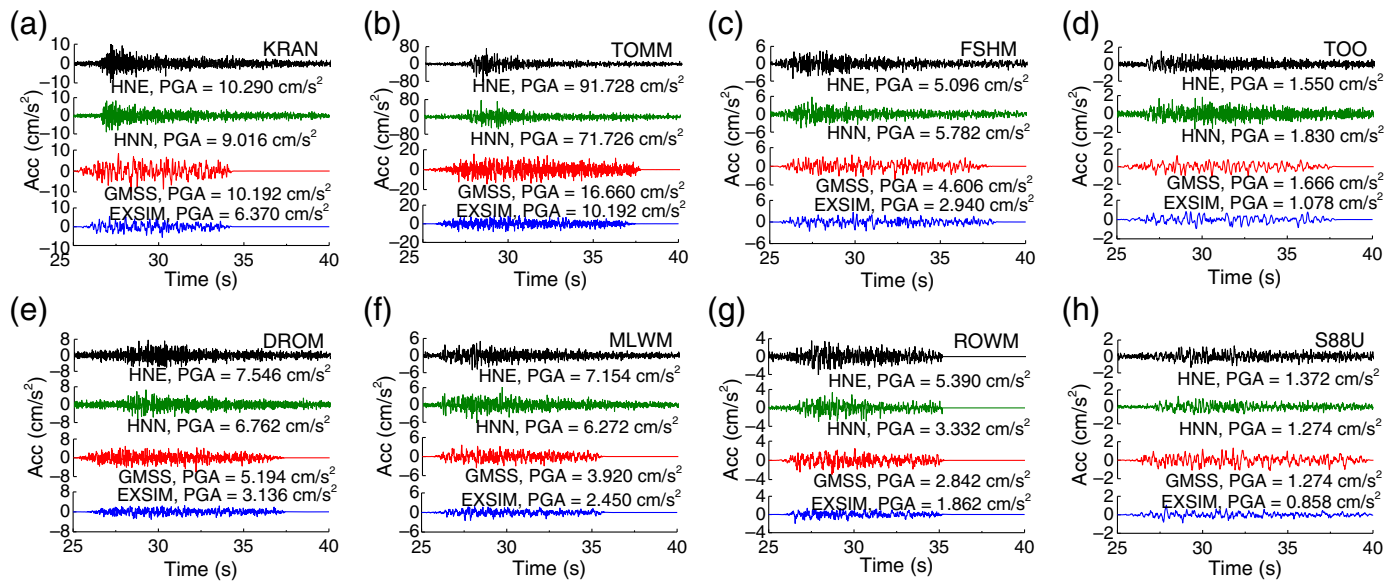


**Figure 7.** Horizontal acceleration time series at the selected eight rock sites (panels a–h) during the 2012 Moe earthquake, recorded and simulated by GMSS2.0 and EXSIM. The simulated time series for each station is retrieved

from one single random simulation. The color version of this figure is available only in the electronic edition.

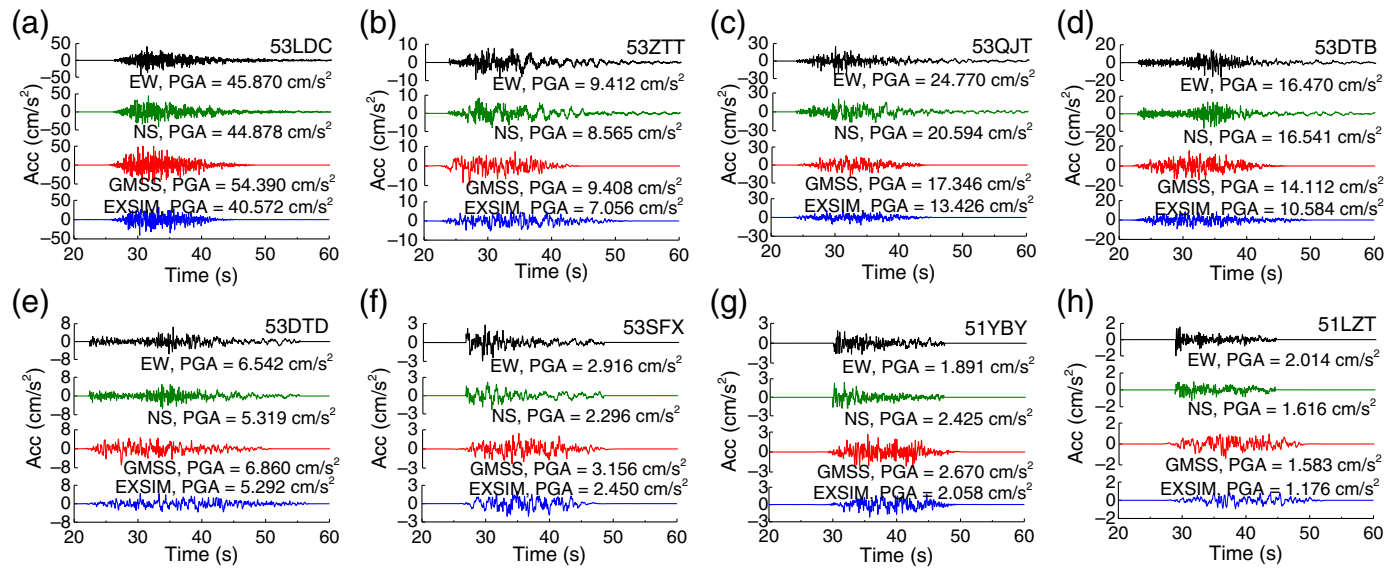


**Figure 8.** Horizontal acceleration time series at the selected eight rock sites (panels a–h) during the 2014 Ludian earthquake, recorded and simulated by GMSS2.0 and EXSIM. The simulated time series for each station is retrieved

from one single random simulation. The color version of this figure is available only in the electronic edition.

larger than that given by GMSS2.0, and this is because the source-duration model used in EXSIM (equation 22) is twice that in GMSS2.0 (equation 16); however, for distances larger than 200 km (including 53SFX, 51YBY, and 51LZT stations), the durations given by the two programs are close to each other, and this is because the duration at large distances is dominated by the path duration ( $T_p$ ) rather than the source duration (this

result is also mentioned in Boore, 2009, p. 3207). To investigate the effect of the source-duration models analyzed in the section earlier, Figure 13b shows the recorded and simulated source duration for each site. According to Figure 13b, both GMSS2.0 and EXSIM underestimate source duration on average for the selected rock sites, and the average relative error is 19.7% and 28.2%, respectively. In contrast with the result shown in

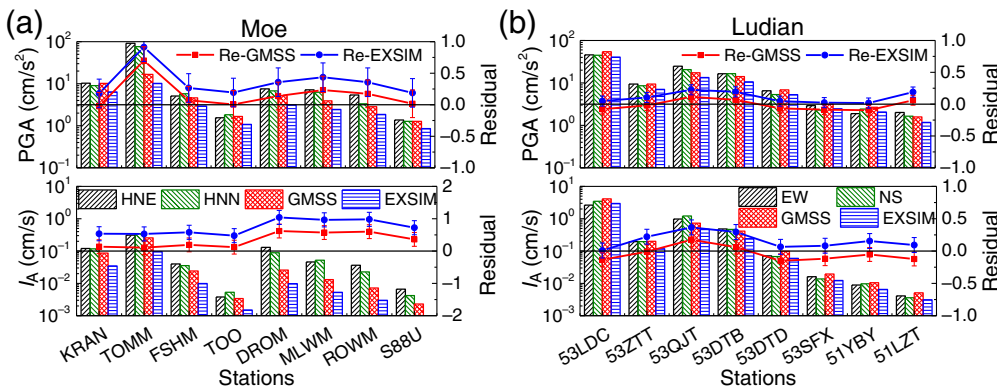


**Figure 9.** Comparison of recorded horizontal peak ground motions with simulated ones by GMSS2.0 and EXSIM for (a) the 2012 Moe earthquake and (b) the 2014 Ludian earthquake. Peak ground acceleration (PGA) and Arias intensity of two horizontal components are compared. Residuals are calculated using equation (24). The color version of this figure is available only in the electronic edition.

Figure 4, no matter whether for GMSS2.0 or EXSIM, the  $1/f_0$  source-duration model is underestimated compared with the recorded source duration, especially for short to intermediate distances ( $<100$  km). The main reason for the conflicting results is that the number of sample sites for the 2014 Ludian earthquake is too small (only 8), whereas the  $1/f_0$  or  $0.6/f_0$  model is concluded from the average of a large number of simulations. More work needs to be conducted on this topic in future studies.

As mentioned earlier, for the 2012 Moe earthquake, the fault dimension is much smaller than the 2014 Ludian earthquake, and the rupture velocity of the 2012 Moe earthquake is larger than that of the latter event. Therefore, the calculated source duration of the 2012 Moe earthquake is apparently

smaller than that of the 2014 Ludian earthquake, and the corner frequency is larger. This results in the difficulty in picking the source duration ( $T_0$ ) out from the whole duration ( $T_d$ ) for the Moe event. For these reasons, durations of the 2012 Moe earthquake are not discussed in this part.

An additional comparison between the simulations and existing GMMs is provided in this section. In this comparison analysis, the ground motions given by the selected GMMs are mainly used as the regional benchmark to validate the reliability of the simulations. The detailed information of the selected GMMs is listed in Table 6.

In the selected GMMs, the TLT20 model is a regionally adjustable GMM (typically for low-to-moderate seismicity regions) that is developed using a data set generated by stochastic ground-motion simulations, with a point source model and generic local crustal model (Tang *et al.*, 2019; Tang, Lam, *et al.*, 2020; Tang, Xiang, *et al.*, 2020; Tang *et al.*, 2021). LZW18 model is an empirical GMM developed specifically for the Yunnan and Sichuan regions, using a strong-motion data set containing 276 recordings from 22 earthquake events (including the 2014 Ludian earthquake) (Li *et al.*, 2018). YA15 model is a generic regionally adjustable GMM developed

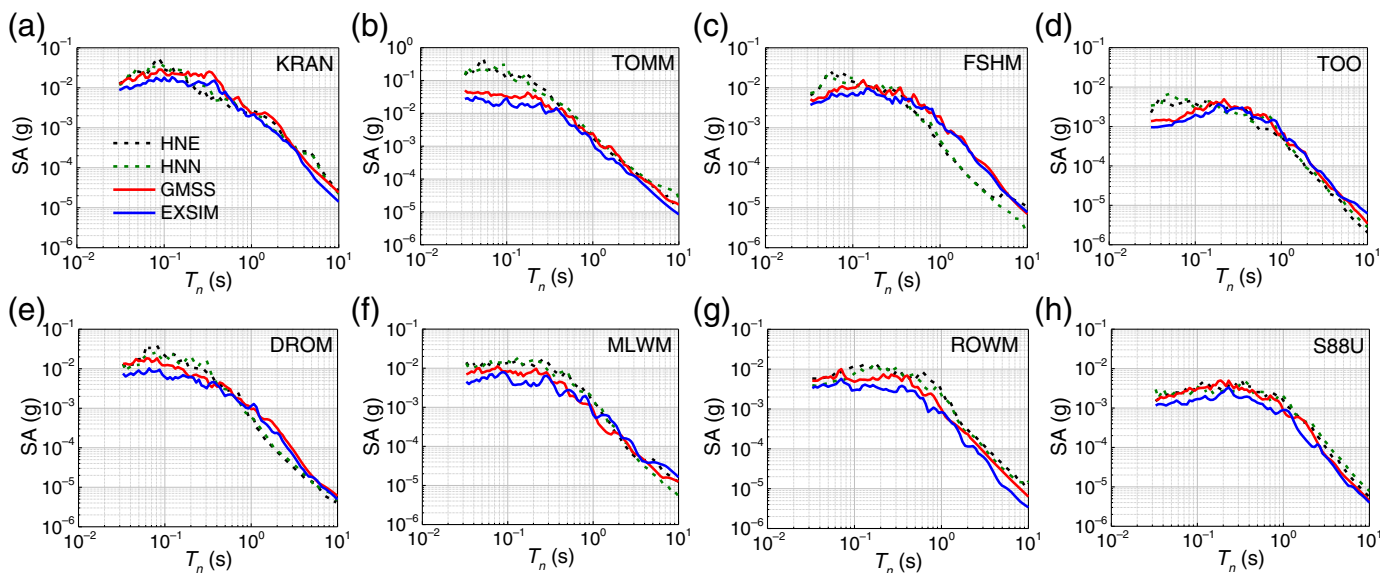
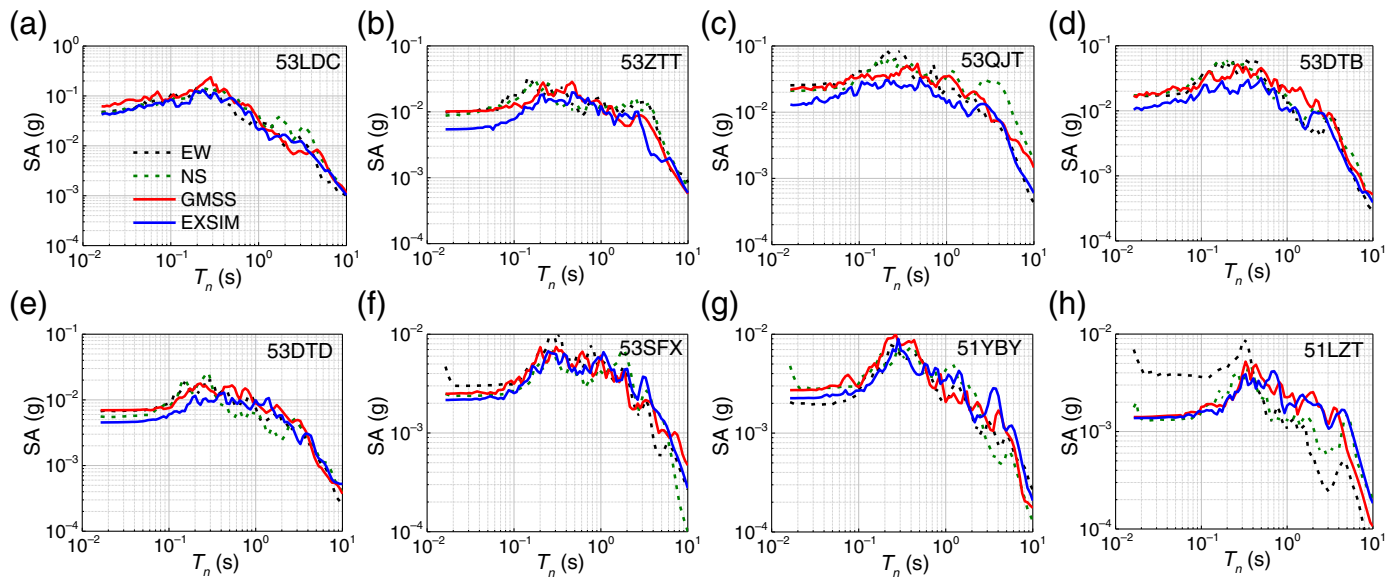


**Figure 10.** Horizontal 5%-damped pseudoacceleration response spectra (SA) at the selected eight rock sites (panels a–h) during the 2012 Moe earthquake, recorded and simulated by GMSS2.0 and EXSIM. The simulated

SA for each station is retrieved from one single random simulation. The color version of this figure is available only in the electronic edition.



using the equivalent point source model (Yenier and Atkinson, 2015) and a third-party semi-empirical site amplification model (Seyhan and Stewart, 2014). YCL14 is a regional empirical model specifically developed for the Yunnan and Sichuan regions, using a data set containing 332 recordings from 24 earthquake events (Yu *et al.*, 2014). CY14 model is a widely used Next Generation Attenuation-West 2 GMM and is typically developed for California in western North America (Chiou and Youngs, 2014). A12 is a finite-fault simulation-based GMM developed specifically for SEA (Allen, 2012), using the input parameters obtained from 1079 strong- and weak-motion records from 75 earthquake events. SGC09 is a broadband simulation-based GMM developed for several regions in Australia, using the regional crustal models and earthquake source scaling relations (Somerville *et al.*, 2009). Finally, the AB06 model is developed from a data set generated from stochastic simulations using a finite-fault source model and an empirical crustal amplification model for eastern North America (Atkinson and Boore, 2006). These GMMs are developed via different techniques and for different regions, and they are employed in this article as the regional benchmark of ground shaking level. The comparison results are shown in Figures 14 and 15.

As mentioned earlier, the ground motions predicted by the selected GMMs are used as benchmarks of the regional ground-motion level, and thus the shaded area can be utilized to validate the simulated ground motions. For the 2012 Moe earthquake (Fig. 14), most

**Figure 11.** Horizontal 5%-damped SA at the selected eight rock sites (panels a–h) during the 2014 Ludian earthquake, recorded and simulated by GMSS2.0 and EXSIM. The simulated SA for each station is retrieved from one single random simulation. The color version of this figure is available only in the electronic edition.

ground motions simulated by GMSS2.0 (and the recorded ones) are within the acceptance range, indicating that the simulated ground motions are reliable. For the 2014 Ludian earthquake (Fig. 15), the ground motions at long periods ( $>1.0$  s) show apparent higher amplitudes (and high variances) for the entire distance range, compared with the predictions of the selected GMMs (including the two regional GMMs specific for the Yunnan and Sichuan regions), indicating that more work needs to be performed in selecting suitable GMMs to represent the ground motions characteristic for this region. The high amplitudes at long periods for this event can be well

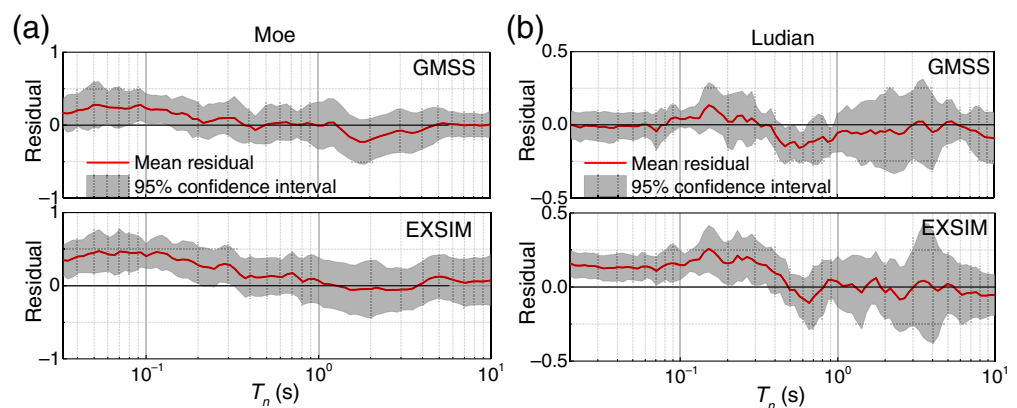


**Figure 12.** Residuals for horizontal SA at selected eight rock sites during (a) the 2012 Moe earthquake and (b) the 2014 Ludian earthquake. Residuals are calculated using equation (24). The color version of this figure is available only in the electronic edition.

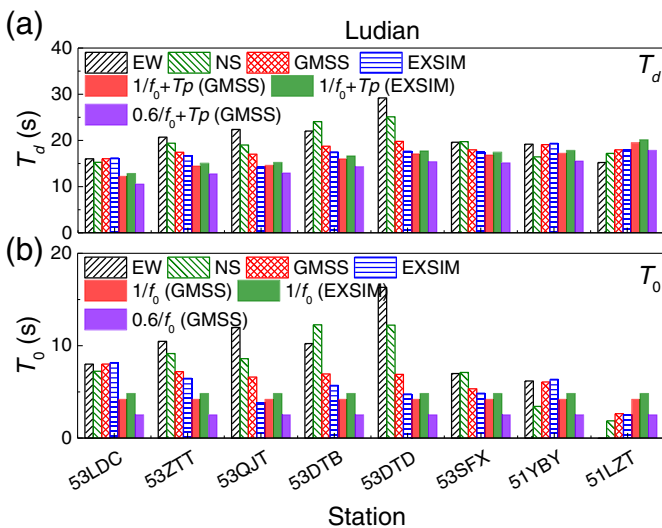


**Figure 13.** Horizontal ground-motion duration (a)  $T_d$  and (b)  $T_0$  at the selected eight rock sites during the 2014 Ludian earthquake, recorded and simulated by GMSS2.0 and EXSIM (averaging 20 simulations over 50 random hypocenters). In panel (a),  $T_p$  refers to path duration and is calculated using the effective distances ( $R_{\text{eff}}$ ) given in Table 4 and the model in Table 5.  $f_0$  is the corner frequency, and the value is 0.3525 and 0.306 for GMSS2.0 and EXSIM, respectively. The color version of this figure is available only in the electronic edition.

explained by the site amplification shown in Figure 6b, which shows obvious peaks at low frequencies in the HVSR curves. This phenomenon is mainly due to the shear-wave velocity contrast at deep depths, and this low-frequency peak can also be found in the HVSR curve of the AKTH19 station in Japan (Zhu *et al.*, 2020, fig. 3, p.4).

For both events, GMSS2.0 performs better than EXSIM in simulating the ground motions at the select stations, which is evidenced by the fact that GMSS2.0 can give closer estimates

(red circles) to the field recordings (black and green squares) than EXSIM (blue circles) at all selected stations.

## DISCUSSIONS AND CONCLUSIONS

According to Brune (1970) and Beresnev (2002), the corner frequency is equivalent to the source duration in the frequency domain, and its value is proportional to the reciprocal of source duration. Therefore, both of them are the key parameters to determine the ground-motion levels. The modeling of corner frequency (same as source duration) has attracted more attention from scholars recently. For example, Cao *et al.* (2021) proposed an approach for constructing a slip-correlated corner frequency (SCF), and they concluded that SCF performs quite well compared with the dynamic corner frequency (used in this study). The updated model proposed by this study is, in fact, similar to Cao *et al.* (2021) as the author incorporated the rupture velocity, which impacts the slip during an earthquake, into the corner-frequency modeling process (Beresnev and Atkinson, 1997).

By definition, the source duration is the time of the average slip reaching its final value (expressed as a fixed fraction of  $\bar{u}(\infty)$ ) from zero at a point on the rupture plane during an earthquake event. For a single subfault, the average slip is defined as half of the circular radius in this study, and equation (16) is used for calculating the source duration for subfault. By contrast, the currently distributed EXSIM uses equation (22) to calculate the source duration for a single subfault. Whether equation (16) or (22) (defined as the original source-duration model), the source duration calculated by these equations for a single subfault should be more accurate than any models based on corner frequency (e.g.,  $1/f_0$ ), as there are large discrepancies between the original source duration and corner-frequency-based source duration (as shown in Fig. 4 in this study and fig. 10 in Boore, 2009, p. 3211).

TABLE 6  
Selected Ground-Motion Models (GMMs) for Comparison Purpose

Number	GMM	Region	Type	Distance	Reference
1	TLT20*	Regionally adjustable	Purely simulated (point source)	$R_{\text{eff}}$	Tang, Lam, <i>et al.</i> (2020)
2	LZW18	Yunnan and Sichuan	Empirical	$R_{\text{rup}}$	Li <i>et al.</i> (2018)
3	YA15*	Regionally adjustable	Purely simulated (equivalent point source)	$R_{\text{rup}}$	Yenier and Atkinson (2015)
4	YCL14	Yunnan and Sichuan	Empirical	$R_{\text{epi}}$	Yu <i>et al.</i> (2014)
5	CY14*	Western North America	Empirical	$R_{\text{rup}}$	Chiou and Youngs (2014)
6	A12	Southeastern Australia	Semi-simulated (finite-fault source)	$R_{\text{rup}}$	Allen (2012)
7	SGC09	Australia	Semi-simulated (broadband)	$R_{\text{JB}}$	Somerville <i>et al.</i> (2009)
8	AB06*	Eastern North America	Semi-simulated (finite-fault source)	$R_{\text{rup}}$	Atkinson and Boore (2006)

\*Used for comparison in both 2012 Moe and 2014 Ludian earthquakes.

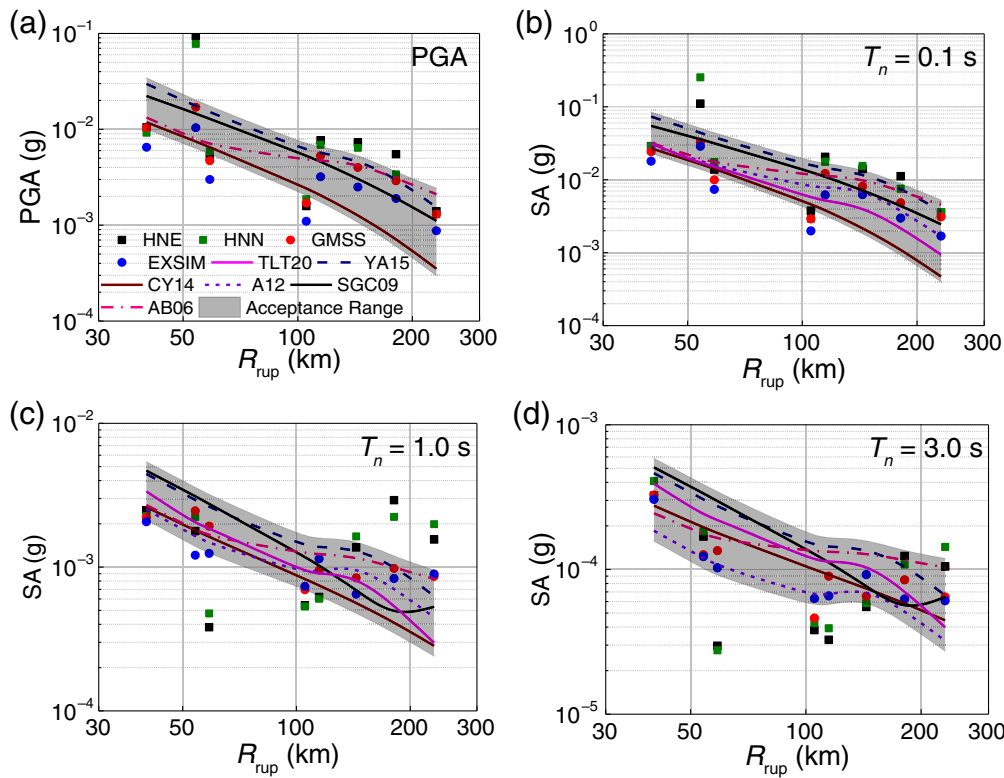


**Figure 14.** (a) Horizontal PGA and 5%-damped SA at (b) 0.1, (c) 1.0, and (d) 3.0 at the selected stations on rock sites during the 2012 Moe earthquake, recorded and simulated by GMSS2.0 and EXSIM (average of 20 simulations over 50 random hypocenters), as well as the predictions of six ground-motion models (GMMs) for each event. Because the TLT20 and A12 model do not provide PGA predictions, there is no line for this model in the PGA subplot. The shaded area indicates the acceptance range of regional ground motions defined by the selected GMMs, according to the criteria proposed by Goulet *et al.* (2015). The color version of this figure is available only in the electronic edition.

The influence of the subfault size on the source duration is also investigated in this study. The author investigated the simulated duration for M 7 and 8, using the parameters listed in Table 2, with four different subfault sizes ( $2 \times 2$ ,  $4 \times 4$ ,  $6 \times 6$ , and  $8 \times 8$  km). The results show no notable fluctuations in the simulated duration (both  $T_{5-75}$  and  $T_{5-95}$ ), indicating the ground-motion duration is not sensitive to the subfault size. This result is basically because of the use of the scaling factor (which is based on the acceleration spectra rather than velocity spectra) in the program (Boore, 2009), and this scaling factor functionates similarly with the source-duration constraint in the deterministic kinematic source models (Cao *et al.*, 2021).

Another point that needs to be cleared is the stress-drop value used to simulate the ground motions on rock sites during the studied events. As mentioned in many studies, there are large variances in determining the stress-drop value. For the 2012 Moe earthquake, Attanayake *et al.* (2019) estimated the stress drop of this event as 570 bars on average, based on the information retrieved from the seismic-wave data set and theoretical calculations. However, the “ $k$ ” value in the equation (7) used in their study (Attanayake *et al.*, 2019, p. 4678) can be controversial as

0.38 is used for  $P$  wave rather than  $S$  wave according to Kaneko and Shearer (2014). By contrast, Hoult *et al.* (2021) estimated the stress drop for this event as 290 bars, which is close to the value given by Allen (2012) for shallow earthquakes in SEA (which is 230 bars). But the 2012 Moe earthquake is a typical deep earthquake (with a depth of 17.2 km according to Hoult *et al.*, 2021), which means 500 bars should be used instead of 230 bars according to Allen (2012).

Similarly, for the 2014 Ludian earthquake, according to Liu *et al.* (2014), the whole seismic moment released by this event is  $1.97 \times 10^{18}$  N · m, using the fault dimensions given in Table 5 and equation (2), the stress drop should be 1.97 bars (1 bar = 0.1 MPa), but 28 bars was used as the average value for the same earthquake event in their study (and this value is supported by Wang *et al.*, 2021). In addition, according to Cheng *et al.* (2016), the final slip of the 2014 Ludian earth-

quake is around 0.5 m, then the whole seismic moment should be  $1.26 \times 10^{19}$  N · m (using the correlation  $M_0 = \mu A \bar{u}(\infty)$  and assume  $\mu \approx 3.0 \times 10^{10}$  N · m $^{-2}$ ), and the corresponding stress drop will equal 12.61 bars using equation (2).

To sum up, the discrepancies between the theoretical calculation and the value adopted in this study and other studies may come from many sources, and the theoretical calculations can only be approximate as the source and wave-propagation theory is imperfect and wave-propagation media cannot be modeled exactly (the misfits of stress drop can also be partially explained by Atkinson and Beresnev, 1997). For practical engineering requirements, it is a good way to quantify the range of the parameters to capture the uncertainties in ground-motion simulations. In fact, all the input parameters used in the stochastic ground-motion simulations, including the fault dip, azimuth angle, stress drop, pulsing percentage, geometric spreading function, quality factor,  $\kappa_0$  value, and so on, can be treated as probability distributions to capture the aleatory uncertainties, like normal or uniform distribution (Atkinson and Boore, 2006). However, for the length limit, the uncertainties of the parameters are not discussed in depth in this article.

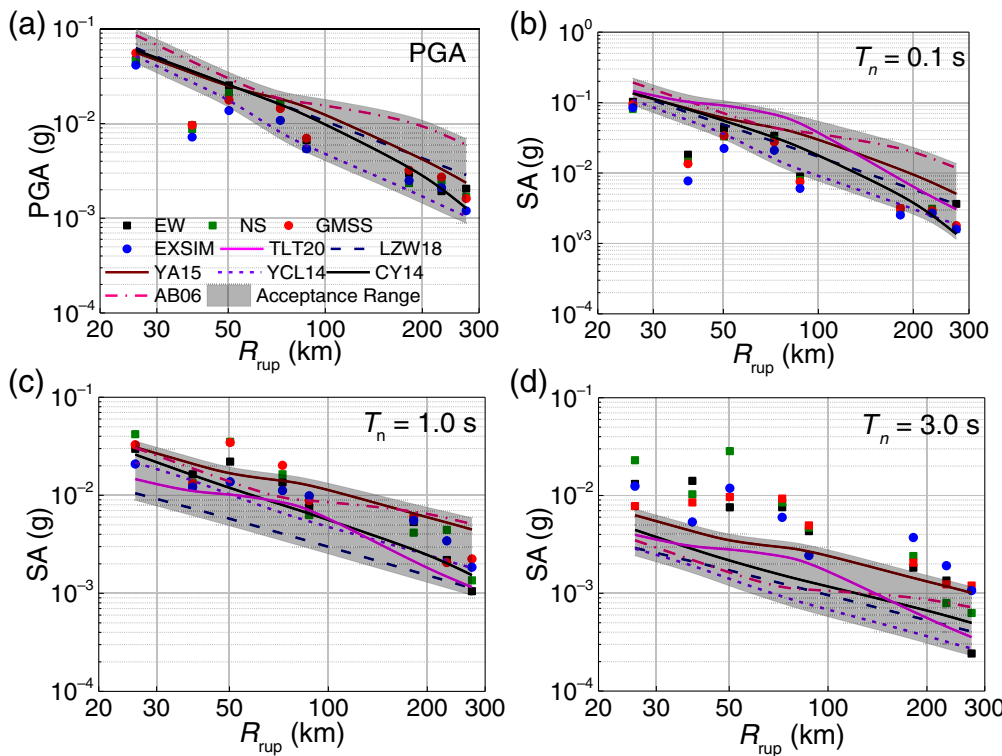


**Figure 15.** (a) Horizontal PGA and 5%-damped SA at (b) 0.1, (c) 1.0, and (d) 3.0 s at the selected stations on rock sites during the 2014 Ludian earthquake, recorded and simulated by GMSS2.0 and EXSIM (average of 20 simulations over 50 random hypocenters), as well as the predictions of six GMMs for each event. Because the TLT20 and A12 model do not provide PGA predictions, there is no line for this model in the PGA subplot. The shaded area indicates the acceptance range of regional ground motions defined by the selected GMMs, according to the criteria proposed by Goulet *et al.* (2015). The color version of this figure is available only in the electronic edition.

The major conclusions of this article are that 1) the updated corner-frequency model provided by this study makes the overall source spectrum modeling theoretically consistent; 2) the  $1/f_0$  source-duration model needs more prudent examinations in practical applications, and this study suggests to use  $0.27/f_0$  and  $0.6/f_0$  as the source-duration model for  $T_{5-75}$  and  $T_{5-95}$  measurements respectively; and 3) the updated corner-frequency model is reliable in practical applications, which is validated by the relatively accurate estimations of ground motions on rock sites during the 2012 Moe and the 2014 Ludian earthquakes.

## DATA AND RESOURCES

The original time series of the studied events in this study are available at <https://github.com/Y-Tang99/Online-Data> (last accessed December 2021). The response spectral data of the Moe earthquake is available at [https://github.com/GeoscienceAustralia/ga-earthquake-hazard/tree/master/2012\\_moe\\_earthquake\\_data](https://github.com/GeoscienceAustralia/ga-earthquake-hazard/tree/master/2012_moe_earthquake_data) (last accessed September 2021). The original Ludian earthquake data for this study is provided by the Institute of Engineering Mechanics (IEM), China Earthquake Administration (under specific application). EXSIM12 is available at <http://www.seismotoolbox.ca> (last accessed March 2021); EXSIM\_DMB is available at [daveboore.com](https://daveboore.com) (last assessed June 2021); The Ground-Motion Simulation System Version 2.0 (GMSS2.0) program

is available at <https://github.com/Y-Tang99/GMSS2.0> (last assessed December 2021). The codes for calculating the effective distance and removing instrument response are available at <https://github.com/Y-Tang99/Online-Code> (last accessed December 2021). The Boore's program can be available at [https://daveboore.com/software\\_online.html](https://daveboore.com/software_online.html) (last accessed June 2021).

## DECLARATION OF COMPETING INTERESTS

The authors acknowledge there are no conflicts of interest recorded.

## ACKNOWLEDGMENTS

The author greatly appreciates the guidance and suggestions provided by David Boore for using EXSIM\_DMB. The author thanks Trevor Allen from Geoscience Australia, Adam Pascale from Seismology Research Center in Australia, and Ryan Hoult from Université Catholique de Louvain in Belgium for providing the 2012 Moe earthquake recording data, and the Institute of Engineering

Mechanics (IEM) in China Earthquake Administration (CEA) for providing the 2014 Ludian earthquake recording data. The author benefits from the communications between Januka Attanayake from The University of Melbourne in Australia to define the Moe earthquake's source parameters. The author also thanks Chuanbin Zhu from GFZ German Research Centre for Geosciences Potsdam in Germany for sharing his experiences in determining the local site amplification factors. Haifeng Zhao from The University of Melbourne in Australia is acknowledged for his help in preparing Figure 5. The Editor-in-Chief Martin Mai and Associate Editor Arben Pitarka are sincerely acknowledged for taking care of this article during the review process. The two anonymous reviewers are thanked for their thoughtful and constructive comments to improve the quality of this article. This work is supported by the Postdoctoral Office of Guangzhou City, China (Grant Number 62104343).

## REFERENCES

- Allen, T. (2012). *Stochastic Ground-motion Prediction Equations for Southeastern Australian Earthquakes using Updated Source and Attenuation Parameters*, Geoscience Australia, Canberra, Record 2012/69.
- Allen, T., P. R. Cummins, T. Dhu, and J. F. Schneider (2007). Attenuation of ground-motion spectral amplitudes in Southeastern Australia, *Bull. Seismol. Soc. Am.* **97**, no. 4, 1279–1292.

- Allmann, B. P., and P. M. Shearer (2009). Global variations of stress drop for moderate to large earthquakes, *J. Geophys. Res.* **114**, no. B1, doi: 10.1029/2008JB005821.
- Atkinson, G. M., and K. Assatourians (2015). Implementation and validation of EXSIM (a stochastic finite-fault ground-motion simulation algorithm) on the SCEC broadband platform, *Seismol. Res. Lett.* **86**, no. 1, 48–60.
- Atkinson, G. M., and I. A. Beresnev (1997). Don't call it stress drop, *Seismol. Res. Lett.* **68**, no. 1, 3–4.
- Atkinson, G. M., and D. M. Boore (1995). Ground-motion relations for eastern North America, *Bull. Seismol. Soc. Am.* **85**, no. 1, 17–30.
- Atkinson, G. M., and D. M. Boore (2006). Earthquake ground-motion prediction equations for eastern North America, *Bull. Seismol. Soc. Am.* **96**, no. 6, 2181–2205.
- Attanayake, J., D. Sandiford, L. S. Schleicher, A. Jones, G. Gibson, and M. Sandiford (2019). Interacting intraplate fault systems in Australia: The 2012 Thorpdale, Victoria, seismic sequences, *J. Geophys. Res.* **124**, 4673–4693.
- Australian Energy Market Operator (AEMO) (2013). Multiple contingency event following an earthquake in Victoria on June 19 2012, Systems Capability, Australian Energy Market Operator, 32 pp.
- Bahrampouri, M., A. Rodriguez-Marek, and R. Green (2021). Ground motion prediction equations for Arias intensity using the Kik-net database. *Earthq. Spec.* **30**, no. 1, 428–448.
- Beresnev, I. A. (2002). Source parameters observable from the corner frequency of earthquake spectra, *Bull. Seismol. Soc. Am.* **92**, no. 5, 2047–2048.
- Beresnev, I. A., and G. M. Atkinson (1997). Modeling finite fault radiation from the wn spectrum, *Bull. Seismol. Soc. Am.* **87**, no. 1, 67–84.
- Beresnev, I. A., and G. M. Atkinson (1998a). Stochastic finite-fault modeling of ground motions from the 1994 Northridge, California, earthquake. I. Validation on rock sites, *Bull. Seismol. Soc. Am.* **88**, no. 6, 1392–1401.
- Beresnev, I. A., and G. M. Atkinson (1998b). FINSIM-a FORTRAN program for simulating stochastic acceleration time histories from finite faults, *Seismol. Res. Lett.* **69**, no. 1, 27–32.
- Boatwright, J., and G. Choy (1992). Acceleration source spectra anticipated for large earthquakes in northeastern North America, *Bull. Seismol. Soc. Am.* **82**, no. 2, 660–682.
- Boore, D. M. (1983). Stochastic simulation of high-frequency ground motions based on seismological models of the radiated spectra, *Bull. Seismol. Soc. Am.* **73**, no. 6(A), 1865–1894.
- Boore, D. M. (2003). Simulation of ground motion using the stochastic method, *Pure Appl. Geophys.* **160**, 635–676.
- Boore, D. M. (2009). Comparing stochastic point-source and finite-source ground-motion simulations: SMSIM and EXSIM, *Bull. Seismol. Soc. Am.* **99**, no. 6, 3202–3216.
- Boore, D. M. (2016). Short note: Determining generic velocity and density models for crustal amplification calculations, with an update of the Boore and Joyner (1997) generic amplification for  $V_s(Z)=760$  m/s, *Bull. Seismol. Soc. Am.* **106**, no. 1, 316–320.
- Brune, J. N. (1970). Tectonic stress and the spectra of seismic shear waves from earthquakes, *J. Geophys. Res.* **75**, no. 26, 4997–5009.
- Brune, J. N. (1971). Correction, *J. Geophys. Res.* **76**, no. 20, 5002.
- Brune, J. N., R. J. Archuleta, and S. Hartzell (1979). Far-field S-wave spectra, corner frequencies, and pulse shapes, *J. Geophys. Res.* **84**, 2262–2272.
- Cao, Z., X. Tao, and Z. Tao (2021). Slip-correlated corner frequency for stochastic finite-fault modeling of ground motion, *Bull. Seismol. Soc. Am.* **111**, no. 2, 723–736.
- Causse, M., and S. G. Song (2015). Are stress drop and rupture velocity of earthquakes independent? Insight from observed ground motion variability, *Geophys. Res. Lett.* **42**, no. 18, 7383–7389.
- Cheng, J., Z. Wu, J. Liu, C. Jiang, X. Xu, L. Fang, X. Zhao, W. Feng, R. Liu, J. Liang, and T. Yang (2015). Preliminary report on the August 3 2014, Mw6.2-Ms6.5 Ludian, Yunnan–Sichuan Border, southwest China, earthquake, *Seismol. Res. Lett.* **86**, no. 3, 750–763.
- Cheng, J., X. Xu, and J. Liu (2016). Cause and rupture characteristics of the 2014 Ludian Ms6.5 mainshock and its aftershock distribution using the Coulomb stress changes, *Chin. J. Geophys.* **59**, no. 2, 556–567 (in Chinese).
- Chiou, B. S. J., and R. R. Youngs (2014). Update of the Chiou and Youngs NGA Model for the average horizontal component of peak ground motion and response spectra, *Earthq. Spectra* **30**, no. 3, 1117–1153.
- Chouvet, A., M. Vallée, M. Causse, and F. Courboulex (2018). Global catalog of earthquake rupture velocities shows anticorrelation between stress drop and rupture velocity, *Tectonophysics* **733**, 148–158.
- Dang, P., and Q. Liu (2020). Stochastic finite-fault ground motion simulation for the Mw 6.7 earthquake in Lushan, China. *Nat. Hazards* **100**, 1215–1241.
- Edwards, B., C. Cauzzi, L. Danciu, and D. Fäh (2016). Region-specific assessment, adjustment, and weighting of ground-motion prediction models: Application to the 2015 Swiss seismic-hazard maps, *Bull. Seismol. Soc. Am.* **106**, 1840–1857.
- Goulet, C. A., N. A. Abrahamson, P. G. Somerville, and K. E. Wooddell (2015). The SCEC broadband platform validation exercise: Methodology for code validation in the context of seismic hazard analyses, *Seismol. Res. Lett.* **86**, no. 1, 17–26.
- Hough, S., and D. Dreger (1995). Source parameters of the April 23 1992 M6.1 Joshua Tree, California, earthquake and its aftershocks: Empirical Green's function analysis of GEOS and TERRAscope data, *Bull. Seismol. Soc. Am.* **85**, no. 6, 1576–1590.
- Hoult, R., T. Allen, E. Borleis, W. Peck, and A. Amirsardari (2021). Source and attenuation properties of the 2012 Moe, southeastern Australia, earthquake sequence, *Seismol. Res. Lett.* **92**, 1112–1128,
- Hoult, R. D., A. Amirsardari, D. Sandiford, E. Lumantarna, H. M. Goldsworthy, G. Gibson, and M. Asten (2014). The 2012 Moe earthquake and earthquake attenuation in south eastern Australia, *Australian Earthquake Engineering Society 2014 Conference*, Lorne, Victoria, 21–23 November.
- Irikura, K., and H. Miyake (2011). Recipe for predicting strong ground motion from crustal earthquake scenarios, *Pure and Appl. Geophys.* **168**, no. 2011, 85–104.
- Jayalakshmi, S., J. Dhanya, S. T. G. Raghukanth, and P. M. Mai (2021). Hybrid broadband ground motion simulations in the Indo-Gangetic basin for great Himalayan earthquake scenarios, *Bull. Earthq. Eng.* **19**, 3319–3348.
- Kanamori, H., and D. L. Anderson (1975). Theoretical basis of some empirical relations in seismology, *Bull. Seismol. Soc. Am.* **65**, no. 5, 1073–1095.
- Kaneko, Y., and P. M. Shearer (2014). Seismic source spectra and estimated stress drop derived from cohesive-zone models of circular subshear rupture, *Geophys. J. Int.* **197**, 1002–1015.

- Lam, N. T. K., J. Wilson, and G. Hutchinson (2000). Generation of synthetic earthquake accelerograms using seismological modelling: A review. *J. Earthq. Eng.* **4**, no. 3, 321–354.
- Leonard, M. (2010). Earthquake fault scaling: Self-consistent relating of rupture length, width, average displacement, and moment release, *Bull. Seismol. Soc. Am.* **100**, no. 5A, 1971–1988.
- Li, Y., and G. Wang (2019). Simulation for Ludian (August 3, 2014, Mw 6.2) and Nepal (April 25, 2015, Mw7.) earthquake with improved stochastic point source method, *J. Earthq. Eng.* **23**, no. 7, 1115–1136.
- Li, X., C. Zhai, W. Wen, and L. Xie (2018). Ground motion prediction model for horizontal PGA, 5% damped response spectrum in Sichuan-Yunnan region of China, *J. Earthq. Eng.* **24**, no. 11, 1829–1866 (in Chinese).
- Liu, C., Y. Zheng, X. Xiong, R. Fu, B. Shan, and F. Diao (2014). Rupture process of Ms6.5 Ludian earthquake constrained by regional broadband seismograms, *Chin. J. Geophys.* **57**, no. 9, 3028–3037 (in Chinese).
- Madariaga, R. (1976). Dynamics of an expanding circular fault, *Bull. Seismol. Soc. Am.* **66**, no. 3, 639–666.
- Motazedian, D., and G. M. Atkinson (2005). Stochastic finite-fault modeling based on a dynamic corner frequency, *Bull. Seismol. Soc. Am.* **95**, no. 3, 995–1010.
- Olsen, K. B., and R. Takedatsu (2015). The SDSU broadband ground motion generation module BBtoolbox version 1.5. *Seismol. Res. Lett.* **86**, no. 1, 81–88.
- Ou, G. B., and R. B. Herrmann (1990). A statistical model for ground motion produced by earthquakes at local and regional distances, *Bull. Seismol. Soc. Am.* **80**, no. 6A, 1397–1417.
- Pezeshk, S., A. Zandieh, K. W. Campbell, and B. Tavakoli (2018). Ground-motion prediction equations for central and eastern North America using the hybrid empirical method and NGA-West2 empirical ground-motion models, *Bull. Seismol. Soc. Am.* **108**, no. 4, 2278–2304.
- Sandiford, D. (2013). Seismo-tectonics in southeastern Australia: Insights from the Moe/Thorpdale earthquakes, *B.Sc. Thesis*, School of Earth Sciences, The University of Melbourne, Melbourne, Australia.
- Saragoni, G. R., and G. C. Hart (1974). Simulation of artificial earthquakes, *Earthq. Eng. Struct. Dynam.* **2**, 249–267.
- Sato, T., and T. Hirasawa (1973). Body wave spectra from propagating shear cracks. *J. Phys. Earth.* **21**, 415–431.
- Seyhan, E., and J. P. Stewart (2014). Semi-empirical nonlinear site amplification from NGA West2 data and simulations, *Earthq. Spectra* **30**, 1241–1256.
- Somerville, P., R. Graves, N. Collins, S. G. Song, S. Ni, and P. Cummins (2009). Source and ground motion models for Australian earthquakes, *Australian Earthquake Engineering Society 2014 Conference*, Newcastle, Australia, 11–13 December.
- Su, Y. (2009). Inversion tomography of the seismic wave attenuation (Q value) structure in Yunnan region, *Ph.D. Thesis*, University of Science and Technology of China, Hefei (in Chinese).
- Tang, Y. (2021). GMSS2.0: An enhanced software program for stochastic finite-fault ground motion simulation. *Seismol. Res. Lett.* (Under 2nd round Review).
- Tang, Y., N. Lam, and H. H. Tsang (2021). A computational tool for ground motion simulations incorporating regional crustal conditions, *Seismol. Res. Lett.* **92**, no. 2A, 1129–1140.
- Tang, Y., N. Lam, H. H. Tsang, and E. Lumantarna (2019). Use of macro-seismic intensity data to validate a regionally adjustable ground motion prediction model, *Geosciences* **9**, no. 10, 1–22.
- Tang, Y., N. Lam, H. H. Tsang, and E. Lumantarna (2020). An adaptive ground motion prediction equation for use in low-to-moderate seismicity regions, *J. Earthq. Eng.* doi: [10.1080/13632469.2020.1784810](https://doi.org/10.1080/13632469.2020.1784810).
- Tang, Y., X. Xiang, J. Sun, and Y. Zhang (2020). A generic shear-wave velocity profiling model for use in ground motion simulations, *Geosciences* **10**, no. 10, 408, doi: [10.3390/geosciences10100408](https://doi.org/10.3390/geosciences10100408).
- Wang, Z. (2017). Research on stochastic simulation method for high frequency of ground motions, *Ph.D. Thesis*, Institute of Engineering Mechanics, China Earthquake Administration, Harbin (in Chinese).
- Wang, H., Y. Ren, and R. Wen (2021). A modified stochastic finite-fault method for simulating ground motions in three dimensions: A case study of Ludian earthquake, *Earthq. Eng. Eng. Dynam.* **41**, no. 2, 181–191 (in Chinese).
- Wells, D. L., and K. J. Coppersmith (1994). New empirical relationships among magnitude, rupture length, rupture width, rupture area, and surface displacement, *Bull. Seismol. Soc. Am.* **84**, no. 2, 974–1002.
- Xie, Z., Y. Zheng, C. Liu, X. Xiang, Y. Li, and X. Zheng (2015). Source parameters of the 2014 Ms 6.5 Ludian earthquake sequence and their implications on the seismogenic structure, *Seismol. Res. Lett.* **86**, no. 6, 1–8.
- Xu, Y., R. B. Herrmann, C. Y. Wang, and S. Cai (2010). Preliminary high-frequency ground-motion scaling in Yunnan and southern Sichuan, China, *Bull. Seismol. Soc. Am.* **100**, no. 5B, 2508–2517.
- Xu, X., C. Xu, G. Yu, X. Wu, X. Li, and J. Zhang (2015). Primary surface ruptures of the Ludian Mw6.2 earthquake, southeastern Tibetan Plateau, China, *Seismol. Res. Lett.* **86**, no. 6, 1622–1635.
- Yenier, E., and G. M. Atkinson (2015). Regionally adjustable generic ground-motion prediction equation based on equivalent point-source simulations: Application to central and eastern North America, *Bull. Seismol. Soc. Am.* **105**, no. 4, 1989–2009.
- Yu, T., J. Cui, X. Li, and L. Yang (2014). Analysis of ground motion attenuation characterization for moderate earthquakes in the Sichuan-Yunnan region, *Earthq. Res. China.* **30**, no. 3, 409–418 (in Chinese).
- Zhang, Y., Y. Chen, L. Xu, X. Wei, M. Jin, and S. Zhang (2015). The 2014 Mw6.1 Ludian, Yunnan, earthquake: A complex conjugated ruptured earthquake, *Chin. J. Geophys.* **58**, no. 1, 153–162 (in Chinese).
- Zhao, X., J. Liu, and W. Feng (2014). The kinematic characteristics of the Ms6.5 Ludian, Yunnan earthquake in 2014. *Seismol. Geol.* **36**, no. 4, 1157–1172 (in Chinese).
- Zhu, C., M. Pilz, and F. Cotton (2020). Evaluation of a novel application of earthquake HVSR in site-specific amplification estimation, *Soil Dynam. Earth. Eng.* **139**, 106301.

Manuscript received 4 August 2021

Published online 18 January 2022